Article

Cell Reports

Non-conventional Axonal Organelles Control TRPM8 Ion Channel Trafficking and Peripheral Cold Sensing

Graphical Abstract

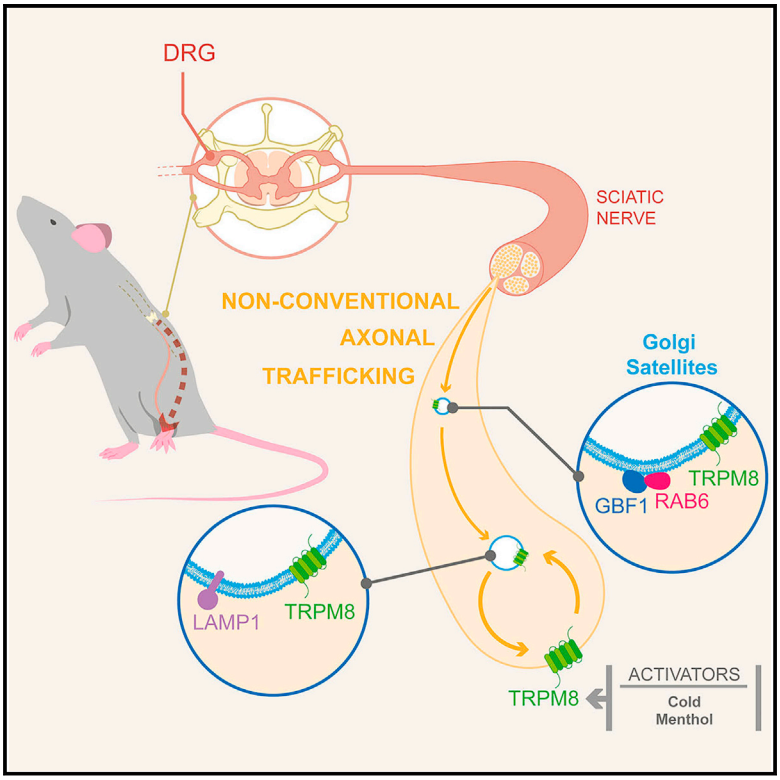

Authors

Víctor Hugo Cornejo, Carolina González, Matías Campos, ..., María Pertusa, Rodolfo Madrid, Andrés Couve

Correspondence

acouve@uchile.cl

In Brief

Cornejo et al. investigate trafficking of cold-sensitive TRPM8 ion channels in peripheral nerves. A non-conventional secretory machinery comprising Golgi satellites, the *trans*-Golgi network, and exocytic vesicles is abundant along primary somatosensory axons and terminals. Inhibition of GBF1 and RAB6 modifies these local secretory organelles, impairing TRPM8-dependent cold sensitivity in mice.

Highlights

- TRPM8 nerve trafficking depends on a non-conventional axonal secretory route
- GBF1 and RAB6 interaction orchestrate axonal Golgi satellites in nerve fibers
- Local disruption of axonal secretory organelles affects TRPM8 cold sensing in mice

Cornejo et al., 2020, Cell Reports *30*, 4505–4517
March 31, 2020 © 2020
https://doi.org/10.1016/j.celrep.2020.03.017

CellPress

Cell Reports
Article

Non-conventional Axonal Organelles Control TRPM8 Ion Channel Trafficking and Peripheral Cold Sensing

Víctor Hugo Cornejo,[1] Carolina González,[1] Matías Campos,[2] Leslie Vargas-Saturno,[1] María de los Ángeles Juricic,[1] Stéphanie Miserey-Lenkei,[3] María Pertusa,[2] Rodolfo Madrid,[2] and Andrés Couve[1,4,*]
[1]Department of Neuroscience and Biomedical Neuroscience Institute (BNI), Facultad de Medicina, Universidad de Chile, Santiago, Chile
[2]Department of Biology, Facultad de Química y Biología, Universidad de Santiago de Chile, and Millennium Nucleus of Ion Channel-Associated Diseases (MiNICAD), Santiago, Chile
[3]Institut Curie, PSL Research University, Sorbonne Université, CNRS, UMR 144, Molecular Mechanisms of Intracellular Transport Laboratory, 75005 Paris, France
[4]Lead Contact
*Correspondence: acouve@uchile.cl
https://doi.org/10.1016/j.celrep.2020.03.017

SUMMARY

TRPM8 is the main ion channel responsible for cold transduction in the somatosensory system. Nerve terminal availability of TRPM8 determines cold sensitivity, but how axonal secretory organelles control channel delivery remains poorly understood. Here we examine the distribution of TRPM8 and trafficking organelles in cold-sensitive peripheral axons and disrupt trafficking by targeting the ARF-GEF GBF1 pharmacologically or the small GTPase RAB6 by optogenetics. In axons of the sciatic nerve, inhibition of GBF1 interrupts TRPM8 trafficking and increases association with the *trans*-Golgi network, LAMP1, and Golgi satellites, which distribute profusely along the axonal shaft. Accordingly, both TRPM8-dependent ongoing activity and cold-evoked responses reversibly decline upon GBF1 inhibition in nerve endings of corneal cold thermoreceptors. Inhibition of RAB6, which also associates to Golgi satellites, decreases cold-induced responses *in vivo*. Our results support a non-conventional axonal trafficking mechanism controlling the availability of TRPM8 in axons and cold sensitivity in the peripheral nervous system.

INTRODUCTION

Neurons are highly specialized cells with a large and morphologically complex architecture composed of somatodendritic and axonal compartments. Axons constitute long and thin cylindrical projections that generate and propagate action potentials. Axon function critically depends on the proteome; therefore, a fundamental question in neurobiology is how the axonal proteome is regulated during development, maturity, and plasticity (Cagnetta et al., 2018; Cornejo et al., 2017). A remarkable control of gene expression, together with various targeting signals, membrane barriers, intracellular filters, and transport mechanisms, determines the selective and timely delivery of proteins to multiple axonal microdomains (Hirokawa and Takemura, 2005; Lasiecka and Winckler, 2011). In addition, the neuron has evolved local and self-regulated biosynthetic and trafficking mechanisms to satisfy the protein composition demands of the axon at significant distances from the cell body. Nevertheless, our understanding of these mechanisms is fragmentary.

One relevant cargo destined for axons of primary somatosensory neurons is the transient receptor potential melastatin 8 ion channel (TRPM8). TRPM8 is a non-selective calcium-permeable cation channel activated by cold and cooling agents such as menthol and icilin (McKemy et al., 2002; Peier et al., 2002; for reviews, see Almaraz et al., 2014, and Madrid and Pertusa, 2014). In cold thermoreceptor neurons (CTNs), cold sensitivity largely depends on the functional expression of TRPM8 (Bautista et al., 2007; Colburn et al., 2007; Dhaka et al., 2007). TRPM8 is involved in the sensation of coolness, detection of skin- and eye-surface dryness, and damage-triggered cold hypersensitivity (González et al., 2017; Parra et al., 2010; Piña et al., 2019; Xing et al., 2007). Despite the relevance of this polymodal ion channel in somatosensory physiology, the molecular mechanisms that govern TRPM8 availability at the plasma membrane of axon terminals remain poorly understood (Ferrandiz-Huertas et al., 2014). Prolonged cold or menthol stimulation increases membrane availability of TRPM8 channels through exocytosis (Toro et al., 2015; Veliz et al., 2010). Vesicle-associated membrane protein 7 (VAMP7), a SNAP receptor (SNARE) that mediates the fusion of lipid bilayers, participates in the exocytosis of TRPM8 through atypical secretory vesicles with lysosomal-associated membrane protein 1 (LAMP1) and an RAB7 molecular identity (Ghosh et al., 2016). However, the earlier axonal secretory system involved in targeting TRPM8 to distant domains and determining cold sensitivity is largely unknown.

Processing stations that govern the trafficking of secreted and transmembrane proteins include the endoplasmic reticulum (ER), the ER-to-Golgi intermediate compartment (ERGIC), and the Golgi apparatus (Luarte et al., 2018; Zhang and Wang, 2016). After ER synthesis and Golgi complex processing, cargo molecules are sorted at the *trans*-Golgi network (TGN) (Guo et al., 2014). The TGN operates as a donor and acceptor compartment in the intracellular trafficking pathway, serving as

an interface between the exocytic and the endosomal systems. In neurons, the sorting machinery at the TGN discriminates between somatodendritic and axonal compartments (Lowenstein et al., 1994; Ye et al., 2007). The unique molecular machinery at the TGN acceptor compartment, in association with motors and cytoskeletal tracks, provides the required specificity in the sorting of TGN vesicles (Horton and Ehlers, 2004; Lasiecka and Winckler, 2011).

Local secretory organelle specializations play a fundamental role in targeting proteins into various neuronal territories (Hanus and Schuman, 2013). In dendrites, the local ER and ERGIC, in addition to TGN-derived vesicles, endocytic components, and other non-conventional organelles, such as Golgi outposts and Golgi satellites, constitute microsecretory stations for transmembrane protein delivery to specialized domains (Bowen et al., 2017; Hanus and Ehlers, 2016; Mikhaylova et al., 2016; Pierce et al., 2001). Enrichment of immature glycosylated membrane proteins highlights the relevance of these local, and possibly abbreviated, pathways (Hanus et al., 2016).

Axons may also use non-conventional organelles to target secreted proteins to the axolemma (González et al., 2018; Jensen et al., 2017). These include the axonal ER, ERGIC, and endocytic organelles (Aridor and Fish, 2009; Farías et al., 2017; González et al., 2016; Merianda et al., 2009; Tsukita and Ishikawa, 1976; Winckler and Yap, 2011; Wu et al., 2017). However, the distribution and roles of essential sorting and modification organelles, such as the Golgi apparatus or TGN counterparts, have remained elusive.

Here we identify the axonal trafficking machinery responsible for TRPM8 delivery in peripheral axons. We demonstrate that function of desomatized corneal cold fibers *ex vivo* and trafficking of TRPM8 surprisingly depend on the axonal ARF-GEF Golgi-specific brefeldin A-resistance factor 1 (GBF1). In agreement with these observations, we show that axonal Golgi satellites are abundant in axons and are sensitive to golgicide A (GCA), a potent and specific pharmacological inhibitor of GBF1. More importantly, we uncover an unexpected trafficking route for TRPM8 that includes the TGN, Golgi satellites, and LAMP1-enriched compartments in the axon. Furthermore, we discover that the small guanosine triphosphatase (GTPase) RAB6, a component that strongly associates to Golgi structures and exocytic vesicles, is a characteristic marker of Golgi satellites in mature axons. Accordingly, we demonstrate that axonal blockade of RAB6 *in vivo* impairs cold responses in mice.

Our results provide compelling evidence for an ensemble of axonal trafficking organelles autonomously controlling the availability and function of TRPM8 channels *in vitro* and *in vivo*, contributing to our understanding of cold sensing in mammals.

RESULTS

Axonal TRPM8 Colocalizes with TGN38 and Is Sensitive to GBF1 Inhibition

Exocytosis of TRPM8 is mediated by the SNARE VAMP7 using non-acidic LAMP1-positive secretory vesicles (Ghosh et al., 2016). To understand the trafficking routes that participate in TRPM8 delivery, we reexamined association to LAMP1 in peripheral axons. To visualize the channels and organelles and to exclude interference of glial components, we used *in vivo* dorsal root ganglia (DRG) electroporation of reporters in adult mouse to generate a non-ambiguous signal (González et al., 2016; Saijilafu et al., 2011). L3 and L4 DRG neurons are the principal contributors that project into the sciatic nerve, innervating the lower limbs. Dissociated sciatic nerve axons were observed after 14 days of reporter expression. TRPM8 localized to discrete and mostly round structures that distributed regularly along non-myelinated axons, which varied in size and intensity (Figures S1A–S1D). We used *in vivo* DRG coelectroporation of a functional TRPM8-YFP fusion channel (Pertusa et al., 2014) and LAMP1-mCherry to evaluate their relative codistribution. TRPM8-positive structures were also positive for LAMP1 and, when not overlapping, were often observed in adjacent structures (Figures S1E, S1G, and S1I). The TGN constitutes a sorting station that localizes to axons (González et al., 2016; Merianda et al., 2009); hence, we also examined whether the distribution of TGN was related to TRPM8 (Mahieu et al., 2007). TGN38-mCherry was chosen because it is a TGN resident integral membrane protein (Roquemore and Banting, 1998). 58% of TRPM8-positive particles overlapped with TGN38 (Figures S1F, S1H, and S1I). These results suggest that the mechanisms of axonal TRPM8 trafficking involve complex organelle interactions, possibly related to Golgi-derived components.

To explore the functionality of Golgi-derived secretory organelles in the trafficking of TRPM8, we used GCA, a potent, highly specific, and rapidly reversible inhibitor of the ARF-GEF GBF1 (Sáenz et al., 2009). GCA disperses and disassembles the Golgi apparatus and TGN structures, arresting secreted and membrane-associated proteins at the ER yet leaving endocytosis and recycling unaffected (Sáenz et al., 2009). We used primary cultures of adult trigeminal ganglia with approximately 10% to 15% of cold-sensitive TRPM8-positive neurons (Madrid et al., 2006; Piña et al., 2019). Cultures were treated for 30 min with GCA (10 μM), because most TRPM8 trafficking to the plasma membrane occurs in this interval (Ghosh et al., 2016; Veliz et al., 2010). A mixed vesicular and tubular TRPM8 expression pattern was visible in control cell bodies, whereas predominantly vesicular distribution dominated their axonal compartments (Figure 1A). Upon GCA treatment, the number of TRPM8-positive particles decreased significantly in the axon (Figure 1A; Figure S2A). In addition, no differences were observed in the soma (Figure S2A). These results unveil a robust trafficking effect of GCA in the axonal organization of TRPM8 channels and suggest that GBF1 may be active in the axon. Indeed, large GBF1-positive particles were abundant in axons, and they drastically decreased after GCA treatment (Figure 1B; Figure S2B). Furthermore, GCA treatment in cultured axons using microfluidic devices induced marked reduction of TRPM8-positive particles in the axonal shaft (Figures S2C and S2D). These results connect axonal GBF1 activity with TRPM8 trafficking.

To determine whether GCA targets the TGN compartment implicated in TRPM8 trafficking, we used heterologous expression in HEK293 cells (Erler et al., 2006; Ghosh et al., 2016; Pertusa et al., 2012; Toro et al., 2015). TRPM8-YFP and TGN38-mCherry partially overlapped under control conditions, and treatment with GCA for 30 min markedly increased colocalization (Figure 1C). Similar results were obtained after expression

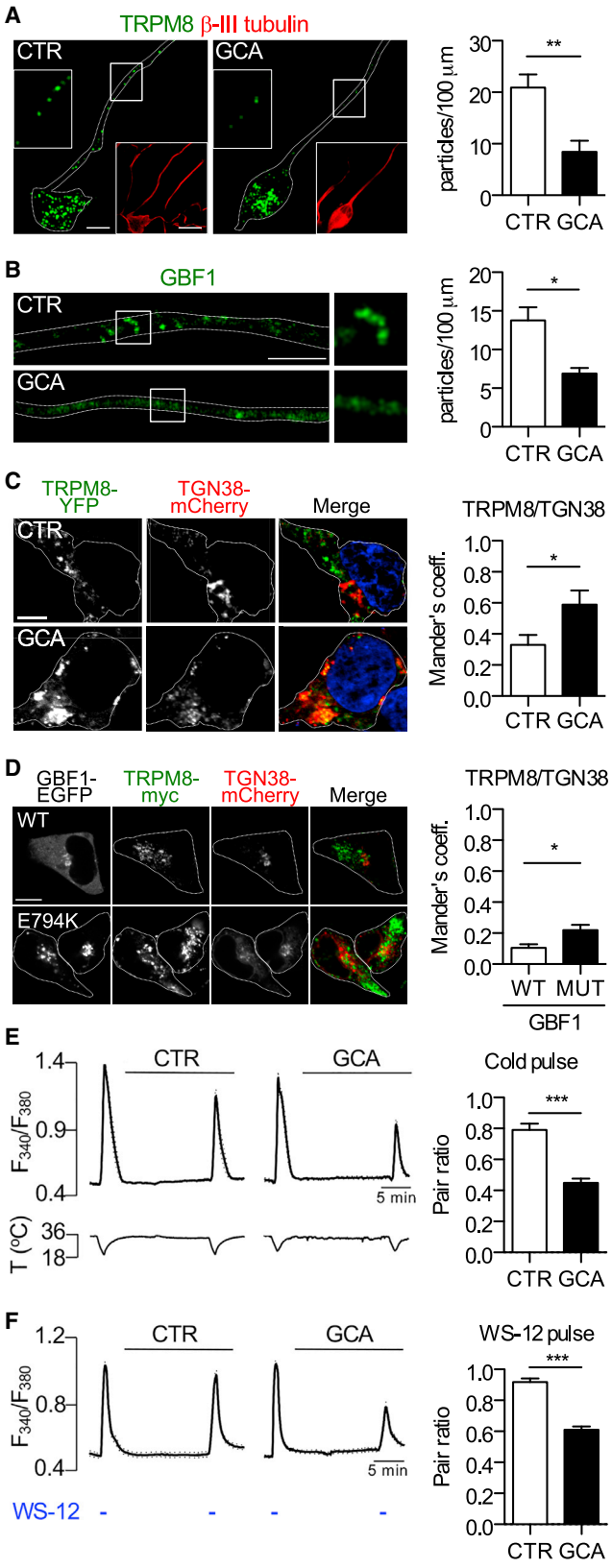

Figure 1. GBF1 Inhibition Alters TRPM8 Distribution and Activity *In Vitro*

(A) Immunofluorescence of endogenous TRPM8 expression in murine primary trigeminal neurons. After 3 days in culture, neurons were treated with GCA (10 μM) for 30 min. The control (CTR) condition was treated with vehicle (0.001% DMSO). The neuron was outlined in white after β-III-tubulin counterstaining. Scale bars: 10 and 20 μm for inset. Right: number of TRPM8-positive particles per axonal length (particles/100 μm). **$p < 0.01$ by Mann-Whitney test; n = 10 cells per group. Data represent mean ± SEM.

(B) Immunofluorescence of endogenous GBF1 expression in murine primary trigeminal neurons, focusing in the axonal protrusion. Scale bar: 10 μm. Right: number of GBF1-positive particles per axonal length (particles/100 μm). *$p < 0.05$ by Mann-Whitney test; n = 10 axons per group. Data represent mean ± SEM.

(C) TRPM8-YFP and TGN38-mCherry were coexpressed in HEK293 cells for 24 h and treated for 30 min with GCA (10 μM) or CTR. Nuclei were counterstained with DAPI (in blue). Scale bar: 10 μm. Right: colocalization analysis of TRPM8-YFP and TGN38-mCherry expressed as Mander's coefficient 1. *$p < 0.05$ by Mann-Whitney test; n = 16 cells for CTR and n = 17 cells for GCA. Data represent mean ± SEM.

(D) Coexpression of TRPM8-myc, TGN38-mCherry, and GBF1-EGFP-WT (wild-type) or mutant GBF1-EGFP-E794K in HEK293 cells for 16 h. TRPM8 was visualized with anti-Myc antibody. Cells were outlined in white by a cellular border in bright field. Scale bar: 10 μm. Right: colocalization analysis of TRPM8-YFP and TGN38-mCherry expressed in Mander's coefficient 1. *$p < 0.05$ by Student's t test; n = 10 cells for both groups. Data represent mean ± SEM.

(E) Calcium imaging of HEK293 expressing TRPM8-YFP channels. The paired-pulse protocol for cold-evoked response was performed in 15 min of treatment with GCA (10 μM) or CTR solution. Top: average (solid line) ± SEM (dotted lines) time course of $[Ca^{2+}]i$ level (F_{340}/F_{380}) in HEK293 cells transfected with TRPM8-YFP (n > 15 cells in each case). Bottom: temperature trace and cold pulse. Scale bar: 5 min. Right: quantification of calcium response in control conditions and GCA for 15 min. ***$p < 0.001$ by Student's t test; n = 38 cells for CTR and n = 35 cells for GCA. Data represent mean ± SEM.

(F) Calcium imaging of HEK293 stably expressing TRPM8-myc. The paired-pulse protocol for WS-12-evoked response was performed in 15 min of treatment with GCA (10 μM) or CTR solution. Left: average (solid line) ± SEM (dotted lines) time course of $[Ca^{2+}]i$ level (F_{340}/F_{380}) in TRPM8-myc HEK293 cells (n > 15 cells in each case). Temperature was maintained at 34°C. Pulses with TRPM8 agonist WS-12 (1 μM) for 1 min were performed. Scale bar: 5 min. Right: quantification of calcium response in control conditions and GCA for 15 min. ***$p < 0.001$ by Student's t test; n = 125 cells for CTR and n = 147 cells for GCA. Data represent mean ± SEM.

of GBF1-E794K, a mutant that inactivates GBF1 (Szul et al., 2005; Figure 1D).

To assess whether blockade of intracellular trafficking relates to changes in TRPM8 expression at the plasma membrane, we used intracellular Ca^{2+} imaging in TRPM8-expressing HEK293 cells (Pertusa et al., 2014, 2018). Increases in the ratio of fluorescence intensities (F_{340}/F_{380}) are indicative of Ca^{2+} entry attributable to TRPM8 opening in response to cold or chemical activators (Figures 1E and 1F). After an initial cold stimulus, cells were treated for 15 min with vehicle or GCA. The second Ca^{2+} elevation was lower in control cells but was further reduced after 10 μM GCA treatment (Figure 1E). In a similar protocol, GBF1 inhibition attenuated intracellular Ca^{2+} rise evoked by the TRPM8 agonist WS-12 (Bödding et al., 2007; Figure 1F). Moreover, absence of the GCA effect with up to 2 min of treatment ruled out that this compound behaves as a TRPM8 antagonist (Figure S2E). Combined, these results support the notion that availability of TRPM8 at the plasma membrane is hampered by GBF1 inhibition and suggest that axonal Golgi-related secretory organelles may be involved in intracellular trafficking.

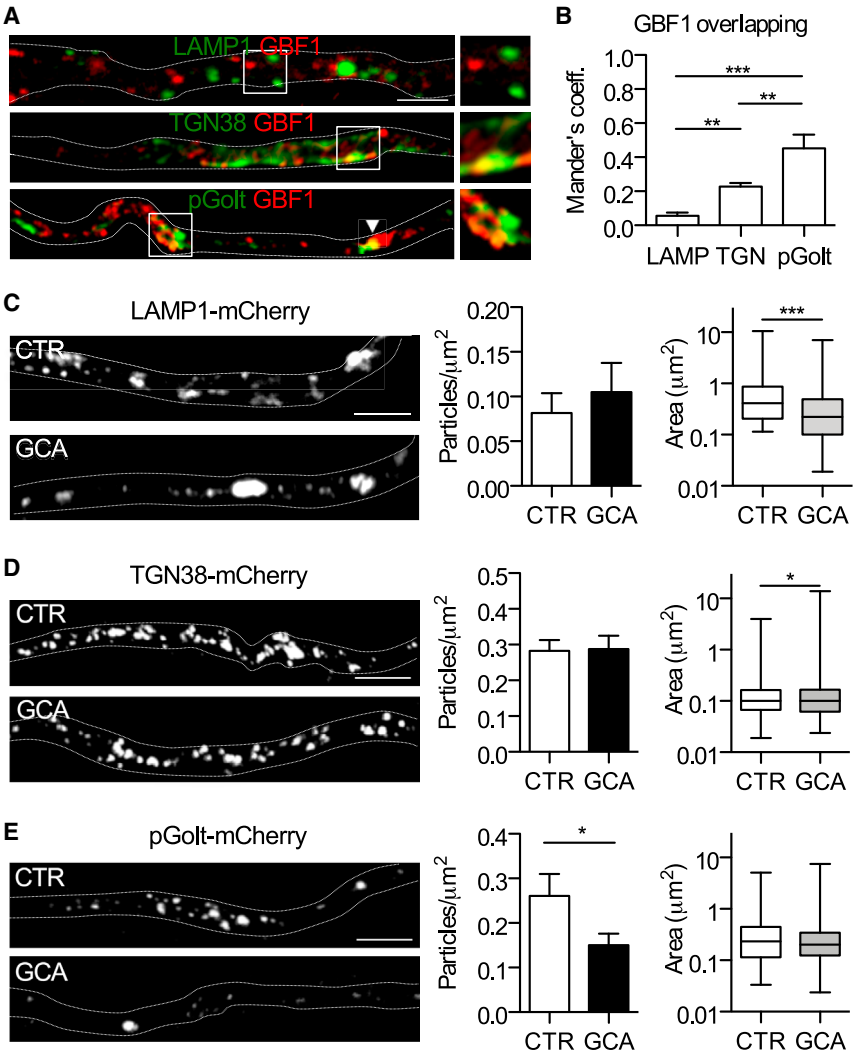

Figure 2. GBF1 Targets Axonal Golgi Satellites *In Vivo*

(A) Immunofluorescence of dissociated sciatic nerve axons for colocalization analysis of endogenous GBF1 and LAMP1, TGN38, and pGolt. Representative images of confocal laser scanning microscopy for each marker are shown. The white square box is magnified on the right. Axons were outlined in white after neurofilament counterstaining. Scale bar: 10 μm.

(B) Colocalization analysis of GBF1 and each of the markers in (A) expressed in Mander's coefficient 1. **$p < 0.01$ and ***$p < 0.001$ by one-way ANOVA and Tukey's test; n = 9 axons for LAMP1, n = 7 axons for TGN38, and n = 4 axons for pGolt. Data represent mean ± SEM.

(C) *In vivo* DRG electroporation of LAMP1-mCherry. 14 days after electroporation, sciatic nerves were dissected and *ex vivo* explants were treated with GCA (20 μM) or CTR media with DMSO (0.002%). Representative images of confocal stacks showing expression in the axoplasm. Scale bar: 10 μm. The number of particles normalized by total area and boxplot of particle area (in micrometers squared) are plotted on the right (n = 5 axons for both groups). ***$p < 0.001$ by Mann-Whitney test. For bar graphs, data represent mean ± SEM.

(D) Same as in (C) for TGN38-mCherry (n = 14 axons for CTR and n = 15 axons for GCA). *$p < 0.05$ by Student's t test.

(E) Same as in (C) for pGolt-mCherry. *$p < 0.05$ by Mann-Whitney test; n = 12 axons for CTR and n = 16 axons for GCA. Data represent mean ± SEM.

GBF1 Associates with TGN and Golgi Satellites in Peripheral Axons *In Vivo*

GBF1 localizes to ERGIC and the *cis*-Golgi interface, where it recruits effectors such as coat protein complex I (COPI) (Szul et al., 2005). Activity of GBF1 may take place directly in axonal Golgi-derived components *in vivo* (González et al., 2016; Merianda et al., 2009). We thus evaluated the distribution of axonal GBF1 in mouse sciatic nerve relative to TGN38 and LAMP1, two elements of TRPM8 trafficking (Ghosh et al., 2016; Mahieu et al., 2007). Colocalization of axonal GBF1 was marginal with LAMP1 and only moderately stronger with TGN38 (Figures 2A and 2B).

Next, we took advantage of a recently described dendritic microsecretory system called Golgi satellites, which labels with pGolt-mCherry, a probe derived from the TGN resident protein

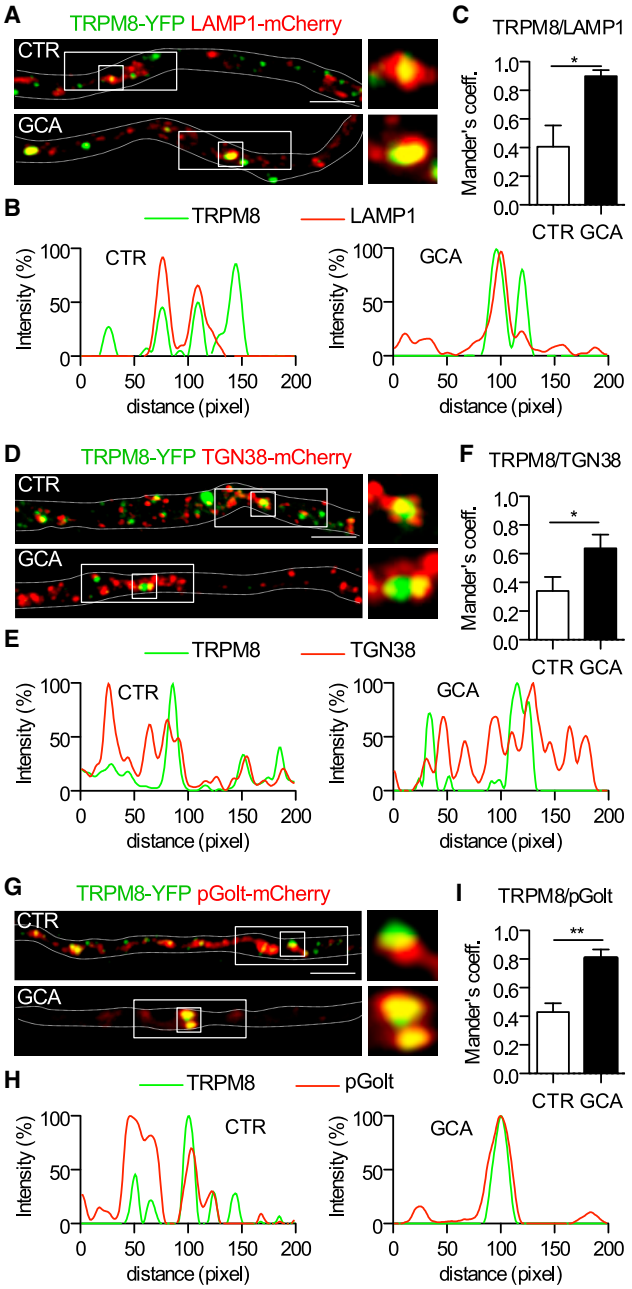

Figure 3. TRPM8 Accumulates in Late Secretory Structures upon *Ex Vivo* GBF1 Inhibition in Axons of the Sciatic Nerve

(A) *In vivo* DRG coelectroporation of TRPM8-YFP and LAMP1-mCherry. 14 days after electroporation, sciatic nerves were dissected and *ex vivo* explants were treated with GCA (20 μM) or CTR media with DMSO (0.002%). Representative images of confocal stacks show expression in the axoplasm. The white square box is magnified on the right. Axons were outlined in white after neurofilament counterstaining. Scale bar: 10 μm.

(B) Expression profiles of normalized fluorescence intensity over distance in pixels of the images in (A). The area of analysis is demarcated in the white rectangle.

(C) Colocalization analysis of TRPM8-EGFP and LAMP1-mCherry (n = 5 axons per group) in Mander's coefficient 1. *p < 0.05 by Mann-Whitney test. Data represent mean ± SEM.

(D–F) Same as in (A–C), respectively, for DRG coelectroporation with TRPM8-YFP and TGN38-mCherry (n = 12 axons per group). *p < 0.05 by Mann-Whitney test.

(G–I) Same as in (A–C), respectively, for DRG coelectroporation with TRPM8-YFP and pGolt-mCherry (n = 11 axons per group). **p < 0.01 by Mann-Whitney test.

calneuron 2 (CALN2) (Mikhaylova et al., 2009, 2016). pGolt-mCherry codistributes with the retromer complex and ERGIC in dendrites. We hypothesized that similar axonal Golgi satellites are implicated in the trafficking of TRPM8. 14 days after *in vivo* electroporation, pGolt-mCherry-positive puncta were abundant in axons (Figure 2A). Structures were discrete, irregular, and often elongated (Figure 2A, inset). The reporter was expressed in myelinated and non-myelinated axons and was partially associated with ERGIC marker p58 (Figures S3A–S3C). Surprisingly, colocalization of pGolt-mCherry with GBF1 was robust (Figures 2A and 2B). To determine the relationship between endogenous Golgi satellites and LAMP1- or TGN38-containing structures, we performed coimmunofluorescence in dissociated axons. A fraction of CALN2 distributed diffusely, whereas another pool showed a discrete pattern (Figure S3D). LAMP1, TGN38, and CALN2 overlapped partially, with noticeable coincidence of TGN38 and CALN2 close to the perimeter of the axon (Figures S3D and S3E). Correspondingly, the distribution of pGolt in HEK293 cells showed remarkable proximity to TRPM8, LAMP1, RAB7, and GBF1 (Figures S3F and S3G).

We subsequently investigated the response of different axonal organelles to GCA when isolated from the somatic compartment. We used an *ex vivo* preparation of electroporated sciatic nerve to analyze the distribution of organelle markers (Figure S4A). Nerve explants were treated in culture with GCA for 1 h, and the size and abundance of structures that contained LAMP1, TGN38, or pGolt were measured. Disassembly of the Golgi apparatus in Schwann cells was used to verify drug activity (Figure S4B). Average abundance of LAMP1- and TGN38-containing structures was unaltered by GCA, yet a significant size reduction of the smaller LAMP1 pool and an increase of the larger TGN38 population were observed (Figures 2C and 2D; Figures S4C–S4F). In contrast, total pGolt-positive particles decreased noticeably after GCA treatment (Figure 2E; Figures S4G and S4H). Overall, this particle analysis suggests that GCA collapses a population of axonal pGolt-containing carriers, affecting the stability of Golgi satellites. Similar results have been reported in dendrites (Mikhaylova et al., 2016). Moreover, because partial overlaps between GBF1 and LAMP1 or TGN38 were observed, these observations point out that GCA affects a subpopulation of both LAMP1- and TGN38-positive intermediaries.

GBF1 Inhibition Produces TRPM8 Accumulation in Multiple Secretory Structures

We next wondered whether intervention by GBF1 inhibition affects TRPM8 trafficking in isolated axons. We coexpressed TRPM8-YFP with LAMP1-mCherry, TGN38-mCherry, or pGolt-mCherry via DRG *in vivo* electroporation, followed by *ex vivo* treatment of nerve explants with GCA for 1 h. As shown in cell cultures, treatment with GCA markedly decreased TRPM8-positive particle density in the axonal shaft, along with a significant increase of particle

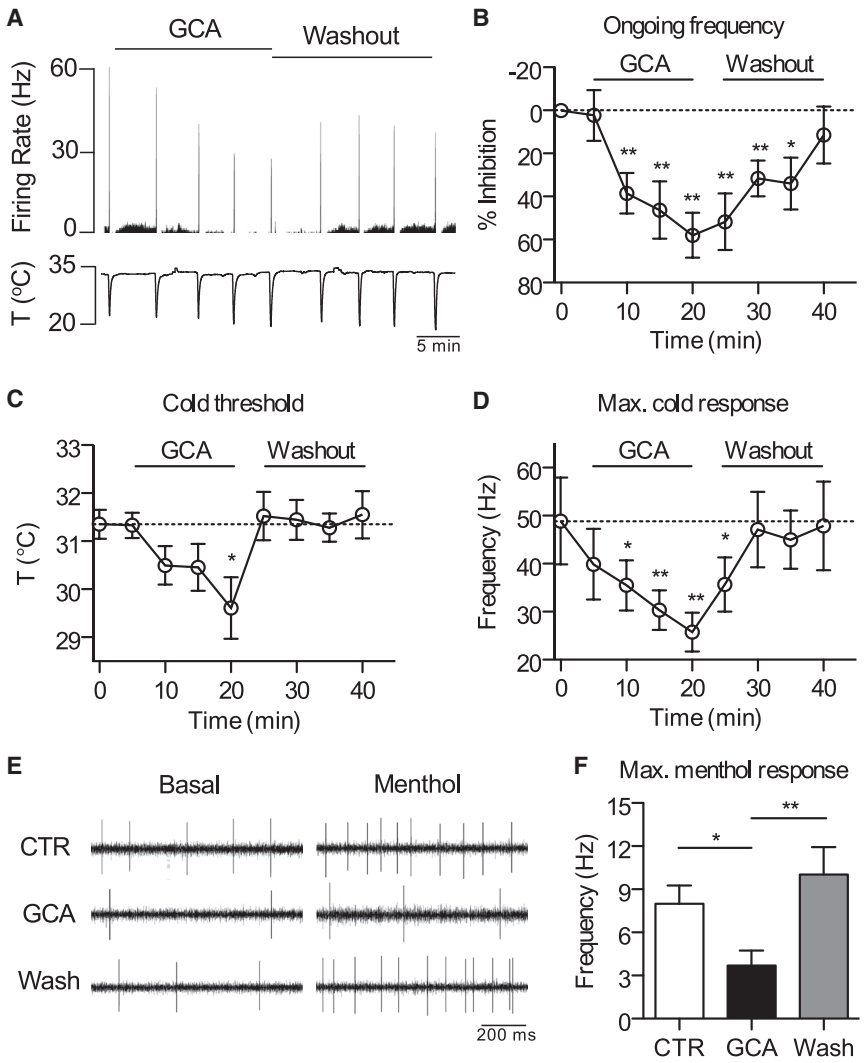

Figure 4. GBF1 Inhibition Reversibly Reduces the Basal Activity and Cold Response of Isolated Corneal CTN Nerve Terminals

(A) Representative firing rate graph of corneal CTNs. 3 min of basal recording was followed by a cold pulse and then GCA treatment (20 μM in recording solution). Washout of GCA was performed after 20 min of treatment. Cold pulsing was performed at 5 min intervals. Scale bar: 5 min.

(B) Percentage inhibition of ongoing frequency activity over time. The percentage inhibition was calculated by subtracting the frequency at each time point (frequency calculated 3 min after cold pulse) from the mean basal frequency of the first 3 min of recording. Time 0 min was assumed to be 0% for graphical representation. *$p < 0.05$ and **$p < 0.01$ by Student's t test; n = 9 terminals. Data represent mean ± SEM here and for (C) and (D).

(C) Cold threshold temperature over time of recording. The average cold thresholds were obtained for each time point of treatment with GCA or washout. *$p < 0.05$ by Student's t test.

(D) Maximum cold frequency triggered by cold pulses over time of recording. The average of maximum frequency reached during cold pulse was obtained for each time point of treatment with GCA or washout. *$p < 0.05$ and **$p < 0.01$ by Student's t test.

(E) Representative recording of NTI activity in corneal CTNs. 3 min basal firing and menthol (20 μM) perfusion for 1 min. Subsequently, eyes were treated for 20 min with GCA (20 μM) and a second menthol application, followed by washout for 20 min and a third menthol application in the absence of GCA. Scale bar: 200 ms.

(F) Maximum firing frequency in menthol (20 μM) before GCA treatment, with 20 min of treatment, and after 20 min of washout. *$p < 0.05$ and **$p < 0.01$ by one-way ANOVA and Tukey's test; n = 8 terminals. Data represent mean ± SEM.

size (Figure S5A). Furthermore, GCA significantly increased colocalization and particle overlap of all secretory components with TRPM8 (Figure 3; Figures S5B–S5D). Higher association with LAMP1 and TGN38 occurred without noticeable changes in the morphology of both positive particles, which is compatible with the absence of change in the number of LAMP1 or TGN38 particles over TRPM8 (Figures S5B and S5C). However, marked condensation of particles was observed for Golgi satellites and TRPM8 (Figure 3G; Figure S5D). GCA also increased the association of TRPM8-YFP and pGolt-mCherry in HEK293 cells (Figures S5F and S5G). These experiments support the notion that local secretory structures, including atypical LAMP1 secretory vesicles, TGN, and Golgi satellites, are sensitive to GBF1 inhibition and govern key steps of TRPM8 trafficking in peripheral axons.

Inhibition of GBF1 Decreases Cold Response and TRPM8-Dependent Ongoing Activity in Corneal CTNs

Corneal CTNs control basal tearing and cold detection, which critically depend on TRPM8 activity (Parra et al., 2010). To study the relevance of local GBF1-dependent TRPM8 trafficking in the physiological responses to cold, we recorded isolated peripheral nerve terminals in the mouse cornea. In this preparation, corneal nerve terminals are separated from their somatic compartments in the trigeminal ganglia. We recorded ongoing nerve terminal impulse (NTI) activity of cold thermoreceptors during cooling ramps and calculated thermal thresholds to evoke NTI frequency changes (cold threshold) and mean increase in action potential firing during temperature drops (maximal cold-evoked response). After a control period, single nerve terminals were treated with GCA for 20 min followed by washout. GCA produced a robust and reversible decrease of the ongoing firing activity (Figures 4A and 4B). Cold threshold and maximum cold-evoked responses were also markedly affected by GCA (Figures 4C and 4D). Menthol, an activator of cold-sensitive afferents through TRPM8 channels, also increases ongoing NTI activity and sensitizes the responses of individual corneal nerve endings to cold temperatures (Parra et al., 2010). Perfusion of 20 μM menthol for 1 min increased NTI activity under control conditions, but GCA

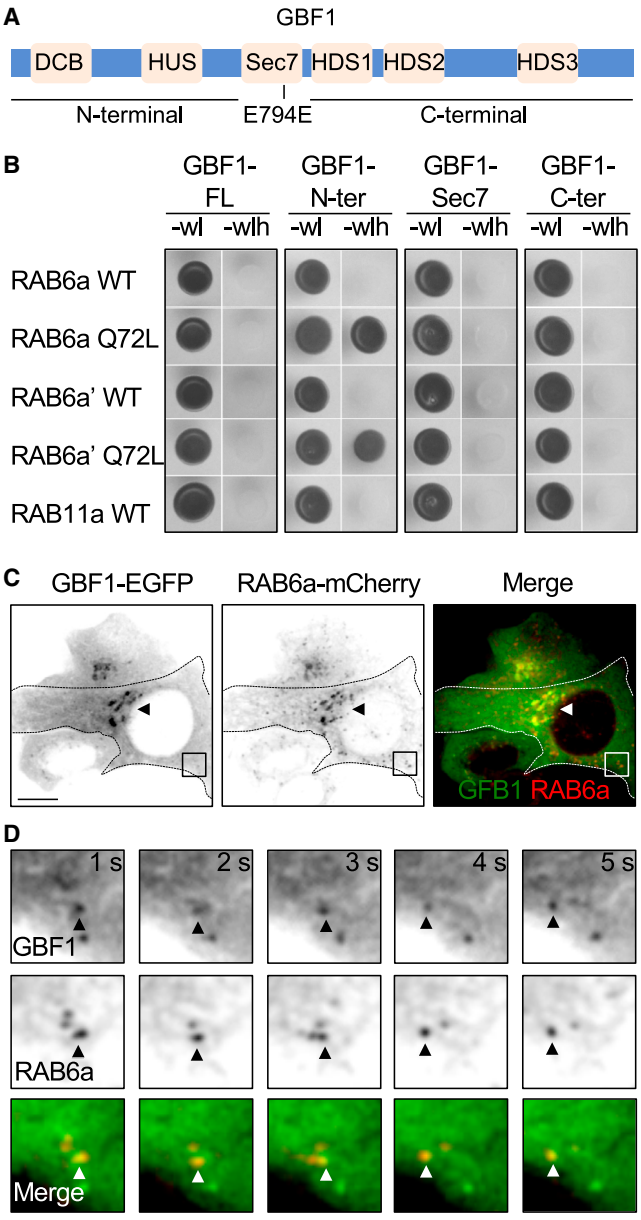

Figure 5. GBF1 Physically Interacts with RAB6

(A) Domain organization of GBF1. The E794E mutation is highlighted. DCB, dimerization and cyclophilin binding; HUS, homology upstream of Sec7; HDS1–HDS3, homology downstream of Sec7.

(B) Y2H interaction between the GBF1 and its fragments (FL, Sec7 domain, and C or N termini) and the active (Q72L) or WT RAB6 isoforms. The *Saccharomyces cerevisiae* reporter strain L40 was cotransformed with plasmids encoding fusion proteins to detect interactions between GBF1 and RAB6. The growth medium lacking histidine (−wlh) indicates interaction.

(C) HeLa cells were cotransfected with GBF1-EGFP and RAB6a-mCherry and imaged every 1 s. The arrowhead indicates the position of the Golgi apparatus. Scale bar: 5 μm.

(D) Magnification of the square box in (C) showing a moving vesicle labeled with GBF1-EGFP and RAB6a-mCherry (arrowhead).

produced a prominent and reversible reduction in firing rate (Figures 4E and 4F). Neither anisomysin nor cycloheximide, classical protein synthesis inhibitors, altered basal terminal activity or cold responses, suggesting that local translation does not contribute to supply newly synthesized TRPM8 channels to the nerve endings (Figure S6). These results indicate that inhibition of GBF1 blocks cold-evoked responses and basal activity of TRPM8-dependent cold-sensitive nerve endings, establishing a local function for GBF1 in channel activity independent of local translation.

GBF1 and Golgi Satellites Associate with the Small GTPase RAB6

RAB6, a small GTPase involved in *cis*-Golgi and medial Golgi trafficking (Miserey-Lenkei et al., 2017), accumulates in pGolt-positive organelles in dendrites (Mikhaylova et al., 2016). In addition, this small GTPase associates with GBF1 at the TGN in photoreceptors (Wang et al., 2017). RAB6 present on TGN-derived carriers regulates exocytosis by enhancing the processive kinesin-dependent motion of secretory vesicles (Grigoriev et al., 2007). Moreover, axonal filtering and transport of secretory RAB6-positive vesicles are regulated in developing neurons (Gumy et al., 2017; Tortosa et al., 2017).

To determine whether RAB6 and GBF1 orchestrate TRPM8 trafficking in peripheral axons, we first explored their interaction via the yeast two-hybrid (Y2H) system. We observed that both RAB6 isoforms, i.e., RAB6a and RAB6a′, in their active form (Q72L, a guanosine triphosphate [GTP]-locked mutant) (Echard et al., 2000) interact with the N-terminal domain of GBF1 (Figures 5A and 5B). No interaction was observed with GBF1 full length (GBF1-FL), possibly because GBF1 truncation unmasks the RAB6-GBF1 interaction domain. RAB11, an endosome-associated small GTPase, was used as a negative control (Figure 5B). As similarly reported for the interaction of GBF1 and the active form of RAB1 (Q67L) (Monetta et al., 2007), GBF1 acts as an effector of RAB6a and RAB6a′ and likely associated with movement of vesicles. To explore this notion in a dynamic state, we employed time-lapse imaging in cultured cells transfected with GBF1-EGFP and RAB6a-mCherry to further analyze their interaction. These proteins codistributed robustly not only in the Golgi apparatus (Figure 5C), but also in peripheral dynamic carriers (Figure 5D).

We then evaluated whether RAB6 associated with the Golgi satellites, LAMP1, and TGN38 in axons of the sciatic nerve. A substantial fraction of RAB6 localized to discrete and sometimes elongated structures. RAB6 partially colocalized with LAMP1 and TGN38 (Figures 6A and 6B). Importantly, colocalization was substantially higher for pGolt, in agreement with the association of pGolt and RAB6 in dendrites (Mikhaylova et al., 2016). We also explored whether GBF1 inhibition altered the organization of RAB6a-positive structures in peripheral axons isolated from their somatic compartments. Abundance of RAB6a-containing structures was significantly increased after *ex vivo* treatment with GCA (Figure 6C), consistent with redistribution of RAB6 into TGN elements and other secretory carriers, as previously shown (Nizak et al., 2003). Furthermore, RAB6a codistributed with TRPM8 in axons, but GCA significantly reduced their association (Figures 6D–6F; Figure S5E). This result indicates that axonal RAB6, characteristic of Golgi satellites and secretory

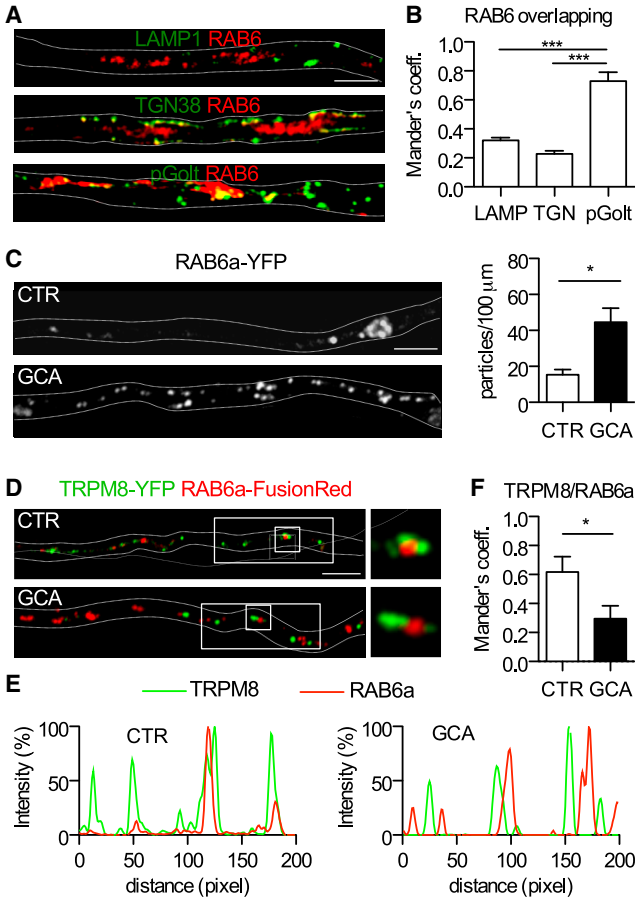

Figure 6. RAB6-Associated Structures Are Sensitive to GBF1 Inhibition

(A) Immunofluorescence of dissociated sciatic nerve axons for colocalization analysis of endogenous RAB6 with LAMP1, TGN38, and pGolt. Immunofluorescence of dissociated sciatic nerve axons. Representative images of confocal laser scanning microscopy for each marker are shown. Axons were outlined in white after neurofilament counterstaining. Scale bar: 10 μm.

(B) Colocalization analysis of RAB6 and indicated markers expressed in Mander's coefficient 1. ***$p < 0.001$ by one-way ANOVA and Tukey's test; n = 8 axons for LAMP1, n = 7 axons for TGN38, and n = 5 axons for pGolt. Data represent mean ± SEM.

(C) *In vivo* DRG electroporation of RAB6a-YFP. 14 days after electroporation, sciatic nerves were dissected and *ex vivo* explants were treated with GCA (20 μM) or CTR media with DMSO (0.002%). Representative images of confocal stacks showing expression in the axoplasm are shown. Scale bar: 10 μm. The number of particles normalized by length in electroporated axons are plotted on the right. *$p < 0.05$ by Mann-Whitney test; n = 4 axons for both groups. Data represent mean ± SEM.

(D) Same as above for TRPM8-YFP and RAB6a-FusionRed. The white square box is magnified on the right. Axons were outlined in white after neurofilament counterstaining. Scale bar: 10 μm. Right inset: zoom of the white box shown on the left.

(E) Expression profiles of normalized fluorescence intensity over distance in pixels of TRPM8-YFP (green line) and RAB6a-FusionRed (red line). The area of analysis is demarcated as a white rectangle.

(F) Colocalization analysis of TRPM8-EGFP and RAB6a-FusionRed, pGolt-mCherry expressed in Mander's coefficient 1. **$p < 0.01$ by Mann-Whitney test; n = 4 axons for both groups. Data represent mean ± SEM.

vesicles, overlaps with TRPM8 in a GBF1-dependent manner in peripheral nerves. Altogether, these observations suggest that GBF1 controls the stability of Golgi satellites, which given their physical association with active RAB6 in this organelle, coordinate the trafficking of TRPM8 in peripheral axons.

Optogenetic Inhibition of RAB6 Reduces Aversive and Menthol-Sensitized Cold Responses *In Vivo*

We explored cold-evoked responses in freely behaving animals using an optogenetic approach based on CRY2-mCitrine and CIB1-FusionRed-RAB6a to interfere acutely with the local function of RAB6 in nerve fibers (Nguyen et al., 2016). Blue illumination induces rapid self-oligomerization and aggregation of CRY2-mCitrine, sequestering CIB1-FusionRed-RAB6a-containing vesicles and disrupting trafficking (Figure 7A). CRY2-mCitrine and CIB1-FusionRed-RAB6a were coelectroporated *in vivo* into DRG. First, excised sciatic nerves from coelectroporated animals were either left in the dark or exposed to blue light for 30 min. In non-illuminated nerves, CRY2-mCitrine appeared homogenously distributed in the axoplasm, and no evident overlap was detected with CIB1-FusionRed-RAB6a (Figure 7B). In contrast, light exposure induced strong aggregation and codistribution with CIB1-FusionRed-RAB6a (Figure 7B, arrowheads). When coexpressed with a functional TRPM8 construct in cell cultures, association of TRPM8- and RAB6a-positive structures was induced by blue light (Figure S7A). CALN2 and GBF1 were more associated with CRY2-mCitrine when coexpressed with CIB1-FusionRed-RAB6a than with RFP in nerve explants (Figures 7C–7H). This confirmed the involvement of RAB6 with GBF1 and axonal Golgi satellites.

Next, *in vivo* coelectroporated animals were evaluated for aversive and menthol-sensitized cold responses. We directed blue light from the bottom of the cage to efficiently illuminate mouse hindpaws, which are directly innervated by electroporated DRG (Figure 7A). CRY2-mCitrine-electroporated animals showed a significant longer latency to aversive response after exposure to blue light compared with EGFP-electroporated mice (Figure 7I). Moreover, after brief sensitization with menthol in the hindpaw, CRY2-mCitrine-electroporated animals exposed to blue light reverted the menthol-induced sensitization in a 10°C cold-plate test (Figure 7J). Importantly, neither animal group showed differential responses upon a hot-plate test (Figure S7B). These results indicate that axonal-localized RAB6a controls cold sensitivity in mice. Collectively, our results demonstrate that Golgi satellites, in association with GBF1 and RAB6, define the availability of TRPM8 channels in nerve endings of CTNs.

DISCUSSION

Neurons have evolved complex and specialized trafficking mechanisms to respond timely to local demands. Axons have developed an intricate organization of organelles that ensure correct protein trafficking and targeting (Cornejo et al., 2017). Here we reveal an additional layer of complexity in the organization of axonal secretory organelles and ion channel delivery in the mature peripheral nervous system. Specifically, we described an ensemble of trafficking intermediaries, which affect TRPM8 trafficking and function *in vitro* and *in vivo*.

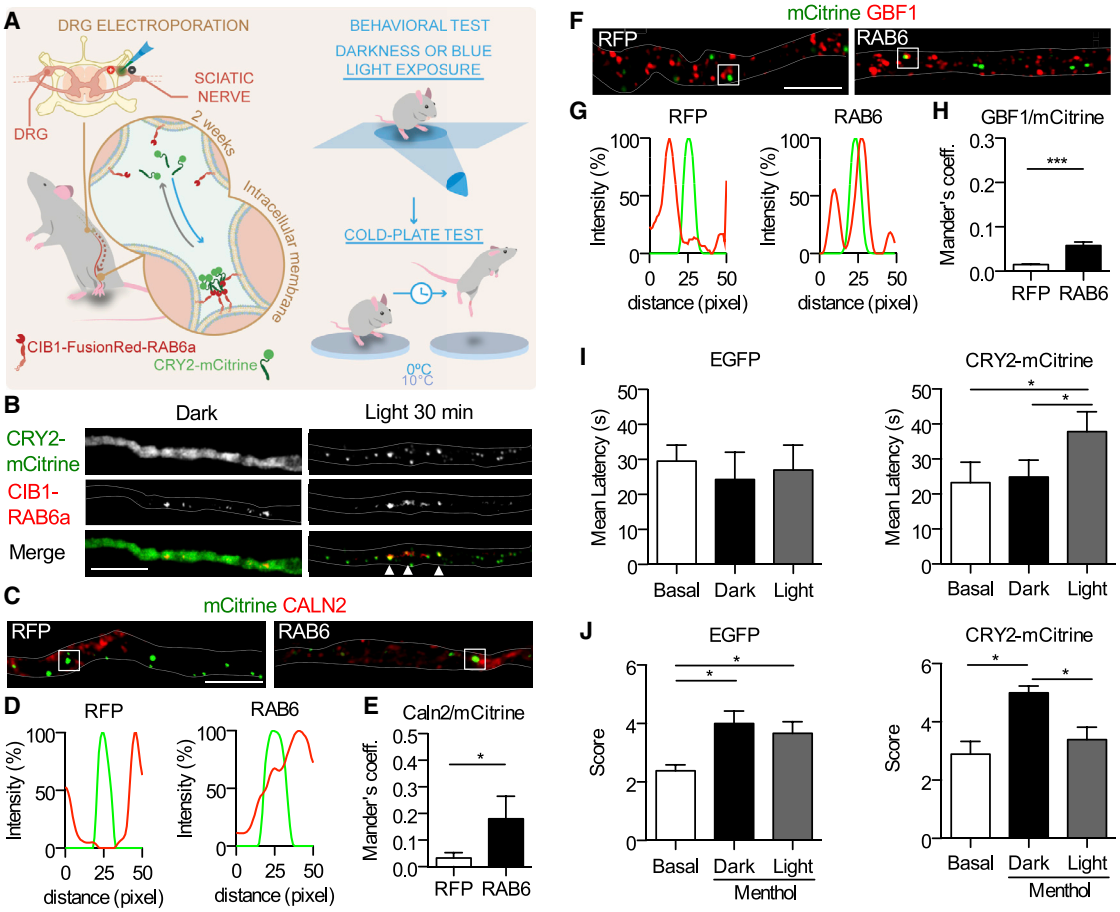

Figure 7. Optogenetic Inhibition of RAB6-Positive Structures in Nerve Terminals Decreases Aversive and Menthol-Sensitized Cooling Responses

(A) Schematic diagram of the protocol to interfere with RAB6 trafficking in axon terminals and behavioral testing. 14 days after *in vivo* CIB1-FusionRed-RAB6a and CRY2-mCitrine or EGFP coelectroporation in left L3 and L4 DRG, cold-plate tests were performed. Cages were exposed from the bottom to light-emitting diode (LED) blue light or left unexposed for 30 min. The plate was set to 0°C or 10°C, and each trial ended when the animal jumped, displaying escape behavior, or showed sensitization behavior with local menthol application on the left hindpaw.

(B) *In vivo* DRG coelectroporation of CRY2-mCitrine and CIB1-FusionRed-RAB6a. 14 days after electroporation, sciatic nerves were dissected and *ex vivo* explants were exposed for 30 min to blue light or maintained in the dark. Representative images of confocal stacks showing expression in the axoplasm of both fluorescent probes are shown. Scale bar: 10 μm.

(C) Immunofluorescence of dissociated sciatic nerve axons for colocalization analysis of endogenous CLN2 and CRY2-mCitrine in the presence of RAB6 or RFP. Representative images of confocal laser scanning microscopy for each marker are shown.

(D) Expression profiles of normalized fluorescence intensity over distance in pixels of CRY2-mCitrine (green line) and CALN2 (red line) for both RFP- and RAB6-expressing axons. The area of analysis is demarcated as a white square in (C).

(E) Colocalization analysis of CALN2 and CRY2-mCitrine expressed in Mander's coefficient 1. *$p < 0.05$ by Mann-Whitney test; n = 8 axons per group. Data represent mean ± SEM.

(F) Same as in (C) for endogenous GBF1 and CRY2-mCitrine in the presence of RAB6 or RFP.

(G) Same as in (D) for CRY2-mCitrine (green line) and GBF1 (red line). The area of analysis is demarcated as a white square in (F).

(H) Same as in (E) for GBF1 and CRY2-mCitrine expressed in Mander's coefficient 1. *$p < 0.05$ by Mann-Whitney test; n = 10 axons per group. Data represent mean ± SEM.

(I) Aversive cold-plate test of mice coelectroporated with CIB1-FusionRed-RAB6a and EGFP (n = 6 animals) or CRY2-mCitrine (n = 10 animals). After room acclimation, animals were tested in a cold plate at 0°C (basal) and then were exposed to dark or blue light for 30 min before a cold-plate test. The time before aversive jump in seconds was quantified. An average of 3 trials on 3 different days was obtained for each animal. *$p < 0.05$ by Friedman and Dunn's test. Data represent mean ± SEM.

(J) Menthol-sensitized cold-plate test of mice coelectroporated with CIB1-FusionRed-RAB6a and EGFP (n = 6 animals) or CRY2-mCitrine (n = 6 animals). Cold-response events of the electroporated left lower limb were monitored at 10°C after local application of menthol in the hindpaw, and an arbitrary score was assigned to the behavior: 0 indicated no response, 1 indicated a lifting response, and 2 indicated licking, brushing, or jumping. Responses were observed during 1 min, and responses were summed to achieve a total number. An average of 3 trials on 3 different days was obtained for each animal. *$p < 0.05$ by Friedman and Dunn's test. Data represent mean ± SEM.

Components of an Axonal Trafficking Route

The composition of the axonal secretory pathway involved in the targeting of secreted and transmembrane proteins has remained controversial (Britt et al., 2016). Evidence from dendrites indicates that neuronal proteins translated locally use the ER and non-canonical Golgi structures that have been detected even in dendritic spines (Bowen et al., 2017). Dendritic Golgi outposts appear to contribute to trafficking and polarization in developing neurons (Hanus and Ehlers, 2016; Ye et al., 2007). Furthermore, Golgi satellites have been recently described to contain some glycosylation machinery needed for transmembrane protein processing, but lack other Golgi markers and the typical cisternae organization of the canonical Golgi apparatus or Golgi outposts (Mikhaylova et al., 2016; Pierce et al., 2001). Our findings indicate that non-conventional organelles may also function in axons and uncover complex and dynamic overlap of trafficking components with no clear carrier identity. Thus, axonal Golgi satellites may function as micro-secretory stations that combine exocytic and partial endocytic capabilities, potentially integrating both pathways. LAMP1 constitutes an exocytic marker of non-conventional secretory vesicles that traffics in Golgi satellites and comprises a cargo protein targeted to the axonal lysosomal pathway from the TGN (Arantes and Andrews, 2006; Caviglia et al., 2016; Chen et al., 2017; Cook et al., 2004). This may reflect the simplification of multiple stages in organelles of mixed identity that distribute throughout the axon.

Studies have reported the widespread distribution of a subset of Golgi-related proteins in distal axons (González et al., 2016; Merianda et al., 2009). However, the structure and molecular signature of Golgi-related compartments is still largely unknown (González et al., 2018). Here we demonstrate that axonal Golgi satellites, similar to the ones described in dendrites, are sensitive to pharmacological inhibitors that target ARF-GEF GBF1 (Mikhaylova et al., 2016). Indeed, their sensitivity to GCA, partial overlap with TGN and LAMP1, and unforeseen strong association to GBF1 justify their classification as distinct and non-conventional organelles. The apparent disassembly of this organelle in response to GCA, which has not been reported previously in axons, may explain the rearrangement of endomembranes in nodes of Ranvier of peripheral myelinated axons upon brefeldin A and GCA treatments (González et al., 2016). Overall, these observations suggest that GBF1 has a pivotal role in controlling local steps of axonal trafficking and endomembrane organization, although indirect effects over two other ARF-GEF targets, namely, BIG1 and BIG2, cannot be ruled out (Lowery et al., 2013). Thus, axons have adapted the machinery classically allocated to the centralized Golgi apparatus to new functions that arise under architectural constrains.

RAB6 is crucial for maintaining the integrity of multiple secretory steps, including exocytosis (Grigoriev et al., 2007). In its GTP-bound conformation, active RAB6 is associated with Golgi membranes and Golgi-derived vesicles and modulates transport and geometry of tubule-vesicular intermediates (Nizak et al., 2003). RAB6 also interacts directly or indirectly with molecular motors to guide targets by microtubules and the actin cytoskeleton, providing support for the functional interaction of cargo trafficking and cytoskeletal motors during secretion, for instance, by directing secretory vesicles from the TGN to the plasma membrane (Matanis et al., 2002; Miserey-Lenkei et al., 2017). Axonal transport and filtering of secretory RAB6-positive vesicles are tightly regulated by MAP2 and MAP6 in the process of neuronal polarization (Gumy et al., 2017; Tortosa et al., 2017). Future work may help determine whether RAB6 and GBF1 interaction in secretory structures contributes to cytoskeleton-dependent movement.

Axonal TRPM8 Trafficking and Cold Sensation

TRPM8 plays a key role in thermotransduction in the somatosensory system. The size of cold-evoked depolarizing currents in cold thermoreceptors depends on the number of functional TRPM8 at the plasma membrane and the intensity of cold stimuli (Madrid et al., 2009; Piña et al., 2019). Consequently, orchestrating an efficient trafficking mechanism to assure availability of TRPM8 is essential to maintain the transduction properties of CTNs at nerve endings. Recent evidence demonstrates that TRPM8 is delivered constitutively in a rapid turnover to the plasma membrane in non-acidic transport vesicles that contain LAMP1 and VAMP7 (Ghosh et al., 2016). Axonal Golgi satellites may regulate the availability of TRPM8 in the proximity of the plasma membrane, but they may also be implicated in vesicle recycling.

Because GBF1 functions mainly in ER-to-Golgi trafficking, we also examined whether local biosynthesis was the source of TRPM8 for local trafficking (Jung et al., 2012). However, our results indicate that TRPM8 is not synthesized locally in axons, at least during the timescale of our experiments. This is in agreement with no transcript for this channel having been detected in isolated axons (Cornejo et al., 2017). Our interpretation is that TRPM8 is delivered constitutively from the somatic compartment and traffics through axonal Golgi-derived organelles for sorting or further processing. In addition, the timing of our experiments suggests that the source of TRPM8 is a ready-to-fuse population of vesicles that rests close to the plasma membrane, but not newly synthesized proteins that would take hours to be processed and inserted into the plasma membrane.

In this work, we provide conclusive evidence supporting the physiological role of late secretory components that affect TRPM8 channel availability and cold transduction in peripheral axons. The sensory information provided by CTNs expressing TRPM8 is necessary for the sensation of coolness of the skin and in the detection of wetness of the ocular surface. Thus, the fine-tuning of TRPM8 channel trafficking is essential to ensure accurate functional output in cold thermoreceptor nerve endings. In this context, our work is a starting point for the exploration of trafficking routes that impinge on cold transduction and thermosensation and of how they can be functionally regulated to explain physiological responses to cold in mammals.

Because TRPM8 is essential for transduction of a rich spectrum of cold temperatures that range from pleasantly cool to outright painful, we venture that trafficking modulation could also be relevant in pathological conditions such as dry eye disease and altered cold sensing in neuropathic and inflammatory pain.

STAR★METHODS

Detailed methods are provided in the online version of this paper and include the following:

- KEY RESOURCES TABLE
- LEAD CONTACT AND MATERIALS AVAILABILITY

SUPPLEMENTAL INFORMATION

Supplemental Information can be found online at https://doi.org/10.1016/j.celrep.2020.03.017.

ACKNOWLEDGMENTS

We thank Romina San Juan for technical support in animal care supervision. We also thank Cathy Jackson (Institut Jacques Monod, France) for providing GBF1 constructs. This work was supported by FONDECYT 3160725 (to V.H.C.), 3160666 (to C.G.), 1161733 (to R.M.), and 1170307 (to A.C.); by DICYT-USACH 021843PP (to M.P.); and by the Iniciativa Cientifica Milenio, Biomedical Neuroscience Institute (ICM P09-015-F to A.C.) and the Millennium Nucleus of Ion Channel-Associated Diseases (MiNICAD) (to R.M. and M.P.). R.M. also thanks the support of VRIDEI-USACH.

AUTHOR CONTRIBUTIONS

Conceptualization, V.H.C., R.M., and A.C.; Formal Analysis, M.d.l.A.J., S.M.-L., C.G., M.C., M.P., and V.H.C.; Investigation, V.H.C., C.G., L.V.-S., S.M.-L., M.C., and M.P.; Writing – Original Draft, V.H.C. and A.C.; Writing – Review & Editing, V.H.C., C.G., M.P., R.M., and A.C.; Visualization, V.H.C. and C.G.; Supervision, R.M. and A.C.

DECLARATION OF INTERESTS

The authors declare no competing interests.

Received: October 9, 2018
Revised: October 7, 2019
Accepted: March 5, 2020
Published: March 31, 2020

REFERENCES

Almaraz, L.M.J., de la Peña, E., and Viana, F. (2014). TRPM8. In Mammalian Transient Receptor Potential (TRP) Cation Channels. Handbook of Experimental Pharmacology, B. Nilius and V. Flockerzi, eds. (Springer).

Arantes, R.M., and Andrews, N.W. (2006). A role for synaptotagmin VII-regulated exocytosis of lysosomes in neurite outgrowth from primary sympathetic neurons. J. Neurosci. *26*, 4630–4637.

Aridor, M., and Fish, K.N. (2009). Selective targeting of ER exit sites supports axon development. Traffic *10*, 1669–1684.

Bautista, D.M., Siemens, J., Glazer, J.M., Tsuruda, P.R., Basbaum, A.I., Stucky, C.L., Jordt, S.E., and Julius, D. (2007). The menthol receptor TRPM8 is the principal detector of environmental cold. Nature *448*, 204–208.

Bödding, M., Wissenbach, U., and Flockerzi, V. (2007). Characterisation of TRPM8 as a pharmacophore receptor. Cell Calcium *42*, 618–628.

Bowen, A.B., Bourke, A.M., Hiester, B.G., Hanus, C., and Kennedy, M.J. (2017). Golgi-independent secretory trafficking through recycling endosomes in neuronal dendrites and spines. eLife *6*, e27362.

Britt, D.J., Farías, G.G., Guardia, C.M., and Bonifacino, J.S. (2016). Mechanisms of Polarized Organelle Distribution in Neurons. Front. Cell. Neurosci. *10*, 88.

Cagnetta, R., Frese, C.K., Shigeoka, T., Krijgsveld, J., and Holt, C.E. (2018). Rapid Cue-Specific Remodeling of the Nascent Axonal Proteome. Neuron *99*, 29–46.

Caviglia, S., Brankatschk, M., Fischer, E.J., Eaton, S., and Luschnig, S. (2016). Staccato/Unc-13-4 controls secretory lysosome-mediated lumen fusion during epithelial tube anastomosis. Nat. Cell Biol. *18*, 727–739.

Chen, Y., Gershlick, D.C., Park, S.Y., and Bonifacino, J.S. (2017). Segregation in the Golgi complex precedes export of endolysosomal proteins in distinct transport carriers. J. Cell Biol. *216*, 4141–4151.

Colburn, R.W., Lubin, M.L., Stone, D.J., Jr., Wang, Y., Lawrence, D., D'Andrea, M.R., Brandt, M.R., Liu, Y., Flores, C.M., and Qin, N. (2007). Attenuated cold sensitivity in TRPM8 null mice. Neuron *54*, 379–386.

Cook, N.R., Row, P.E., and Davidson, H.W. (2004). Lysosome associated membrane protein 1 (Lamp1) traffics directly from the TGN to early endosomes. Traffic *5*, 685–699.

Cornejo, V.H., Luarte, A., and Couve, A. (2017). Global and local mechanisms sustain axonal proteostasis of transmembrane proteins. Traffic *18*, 255–266.

Dhaka, A., Murray, A.N., Mathur, J., Earley, T.J., Petrus, M.J., and Patapoutian, A. (2007). TRPM8 is required for cold sensation in mice. Neuron *54*, 371–378.

Echard, A., Opdam, F.J., de Leeuw, H.J., Jollivet, F., Savelkoul, P., Hendriks, W., Voorberg, J., Goud, B., and Fransen, J.A. (2000). Alternative splicing of the human Rab6A gene generates two close but functionally different isoforms. Mol. Biol. Cell *11*, 3819–3833.

Erler, I., Al-Ansary, D.M., Wissenbach, U., Wagner, T.F., Flockerzi, V., and Niemeyer, B.A. (2006). Trafficking and assembly of the cold-sensitive TRPM8 channel. J. Biol. Chem. *281*, 38396–38404.

Farías, G.G., Guardia, C.M., De Pace, R., Britt, D.J., and Bonifacino, J.S. (2017). BORC/kinesin-1 ensemble drives polarized transport of lysosomes into the axon. Proc. Natl. Acad. Sci. USA *114*, E2955–E2964.

Ferrandiz-Huertas, C., Mathivanan, S., Wolf, C.J., Devesa, I., and Ferrer-Montiel, A. (2014). Trafficking of ThermoTRP Channels. Membranes (Basel) *4*, 525–564.

Ghosh, D., Pinto, S., Danglot, L., Vandewauw, I., Segal, A., Van Ranst, N., Benoit, M., Janssens, A., Vennekens, R., Vanden Berghe, P., et al. (2016). VAMP7 regulates constitutive membrane incorporation of the cold-activated channel TRPM8. Nat. Commun. *7*, 10489.

González, C., Cánovas, J., Fresno, J., Couve, E., Court, F.A., and Couve, A. (2016). Axons provide the secretory machinery for trafficking of voltage-gated sodium channels in peripheral nerve. Proc. Natl. Acad. Sci. USA *113*, 1823–1828.

González, A., Ugarte, G., Restrepo, C., Herrera, G., Piña, R., Gómez-Sánchez, J.A., Pertusa, M., Orio, P., and Madrid, R. (2017). Role of the Excitability Brake Potassium Current I_{KD} in Cold Allodynia Induced by Chronic Peripheral Nerve Injury. J. Neurosci. *37*, 3109–3126.

González, C., Cornejo, V.H., and Couve, A. (2018). Golgi bypass for local delivery of axonal proteins, fact or fiction? Curr. Opin. Cell Biol. *53*, 9–14.

Grigoriev, I., Splinter, D., Keijzer, N., Wulf, P.S., Demmers, J., Ohtsuka, T., Modesti, M., Maly, I.V., Grosveld, F., Hoogenraad, C.C., and Akhmanova, A.

(2007). Rab6 regulates transport and targeting of exocytotic carriers. Dev. Cell *13*, 305–314.

Gumy, L.F., Katrukha, E.A., Grigoriev, I., Jaarsma, D., Kapitein, L.C., Akhmanova, A., and Hoogenraad, C.C. (2017). MAP2 Defines a Pre-axonal Filtering Zone to Regulate KIF1- versus KIF5-Dependent Cargo Transport in Sensory Neurons. Neuron *94*, 347–362.

Guo, Y., Sirkis, D.W., and Schekman, R. (2014). Protein sorting at the *trans*-Golgi network. Annu. Rev. Cell Dev. Biol. *30*, 169–206.

Hanus, C., and Ehlers, M.D. (2016). Specialization of biosynthetic membrane trafficking for neuronal form and function. Curr. Opin. Neurobiol. *39*, 8–16.

Hanus, C., and Schuman, E.M. (2013). Proteostasis in complex dendrites. Nat. Rev. Neurosci. *14*, 638–648.

Hanus, C., Geptin, H., Tushev, G., Garg, S., Alvarez-Castelao, B., Sambandan, S., Kochen, L., Hafner, A.S., Langer, J.D., and Schuman, E.M. (2016). Unconventional secretory processing diversifies neuronal ion channel properties. eLife *5*, e20609.

Hirokawa, N., and Takemura, R. (2005). Molecular motors and mechanisms of directional transport in neurons. Nat. Rev. Neurosci. *6*, 201–214.

Horton, A.C., and Ehlers, M.D. (2004). Secretory trafficking in neuronal dendrites. Nat. Cell Biol. *6*, 585–591.

Jensen, C.S., Watanabe, S., Stas, J.I., Klaphaak, J., Yamane, A., Schmitt, N., Olesen, S.P., Trimmer, J.S., Rasmussen, H.B., and Misonou, H. (2017). Trafficking of Kv2.1 Channels to the Axon Initial Segment by a Novel Nonconventional Secretory Pathway. J. Neurosci. *37*, 11523–11536.

Jung, H., Yoon, B.C., and Holt, C.E. (2012). Axonal mRNA localization and local protein synthesis in nervous system assembly, maintenance and repair. Nat. Rev. Neurosci. *13*, 308–324.

Lasiecka, Z.M., and Winckler, B. (2011). Mechanisms of polarized membrane trafficking in neurons—focusing in on endosomes. Mol. Cell. Neurosci. *48*, 278–287.

Lowenstein, P.R., Morrison, E.E., Bain, D., Shering, A.F., Banting, G., Douglas, P., and Castro, M.G. (1994). Polarized distribution of the *trans*-Golgi network marker TGN38 during the *in vitro* development of neocortical neurons: effects of nocodazole and brefeldin A. Eur. J. Neurosci. *6*, 1453–1465.

Lowery, J., Szul, T., Styers, M., Holloway, Z., Oorschot, V., Klumperman, J., and Sztul, E. (2013). The Sec7 guanine nucleotide exchange factor GBF1 regulates membrane recruitment of BIG1 and BIG2 guanine nucleotide exchange factors to the *trans*-Golgi network (TGN). J. Biol. Chem. *288*, 11532–11545.

Luarte, A., Cornejo, V.H., Bertin, F., Gallardo, J., and Couve, A. (2018). The axonal endoplasmic reticulum: One organelle-many functions in development, maintenance, and plasticity. Dev. Neurobiol. *78*, 181–208.

Madrid, R., and Pertusa, M. (2014). Intimacies and physiological role of the polymodal cold-sensitive ion channel TRPM8. Curr. Top. Membr. *74*, 293–324.

Madrid, R., Donovan-Rodríguez, T., Meseguer, V., Acosta, M.C., Belmonte, C., and Viana, F. (2006). Contribution of TRPM8 channels to cold transduction in primary sensory neurons and peripheral nerve terminals. J. Neurosci. *26*, 12512–12525.

Madrid, R., de la Peña, E., Donovan-Rodriguez, T., Belmonte, C., and Viana, F. (2009). Variable threshold of trigeminal cold-thermosensitive neurons is determined by a balance between TRPM8 and Kv1 potassium channels. J. Neurosci. *29*, 3120–3131.

Mahieu, F., Owsianik, G., Verbert, L., Janssens, A., De Smedt, H., Nilius, B., and Voets, T. (2007). TRPM8-independent menthol-induced Ca2+ release from endoplasmic reticulum and Golgi. J. Biol. Chem. *282*, 3325–3336.

Matanis, T., Akhmanova, A., Wulf, P., Del Nery, E., Weide, T., Stepanova, T., Galjart, N., Grosveld, F., Goud, B., De Zeeuw, C.I., et al. (2002). Bicaudal-D regulates COPI-independent Golgi-ER transport by recruiting the dynein-dynactin motor complex. Nat. Cell Biol. *4*, 986–992.

McKemy, D.D., Neuhausser, W.M., and Julius, D. (2002). Identification of a cold receptor reveals a general role for TRP channels in thermosensation. Nature *416*, 52–58.

Merianda, T.T., Lin, A.C., Lam, J.S., Vuppalanchi, D., Willis, D.E., Karin, N., Holt, C.E., and Twiss, J.L. (2009). A functional equivalent of endoplasmic reticulum and Golgi in axons for secretion of locally synthesized proteins. Mol. Cell. Neurosci. *40*, 128–142.

Mikhaylova, M., Reddy, P.P., Munsch, T., Landgraf, P., Suman, S.K., Smalla, K.H., Gundelfinger, E.D., Sharma, Y., and Kreutz, M.R. (2009). Calneurons provide a calcium threshold for *trans*-Golgi network to plasma membrane trafficking. Proc. Natl. Acad. Sci. USA *106*, 9093–9098.

Mikhaylova, M., Bera, S., Kobler, O., Frischknecht, R., and Kreutz, M.R. (2016). A Dendritic Golgi Satellite between ERGIC and Retromer. Cell Rep. *14*, 189–199.

Miserey-Lenkei, S., Chalancon, G., Bardin, S., Formstecher, E., Goud, B., and Echard, A. (2010). Rab and actomyosin-dependent fission of transport vesicles at the Golgi complex. Nat. Cell Biol. *12*, 645–654.

Miserey-Lenkei, S., Bousquet, H., Pylypenko, O., Bardin, S., Dimitrov, A., Bressanelli, G., Bonifay, R., Fraisier, V., Guillou, C., Bougeret, C., et al. (2017). Coupling fission and exit of RAB6 vesicles at Golgi hotspots through kinesin-myosin interactions. Nat. Commun. *8*, 1254.

Monetta, P., Slavin, I., Romero, N., and Alvarez, C. (2007). Rab1b interacts with GBF1 and modulates both ARF1 dynamics and COPI association. Mol. Biol. Cell *18*, 2400–2410.

Nguyen, M.K., Kim, C.Y., Kim, J.M., Park, B.O., Lee, S., Park, H., and Heo, W.D. (2016). Optogenetic oligomerization of Rab GTPases regulates intracellular membrane trafficking. Nat. Chem. Biol. *12*, 431–436.

Nizak, C., Monier, S., del Nery, E., Moutel, S., Goud, B., and Perez, F. (2003). Recombinant antibodies to the small GTPase Rab6 as conformation sensors. Science *300*, 984–987.

Parra, A., Madrid, R., Echevarria, D., del Olmo, S., Morenilla-Palao, C., Acosta, M.C., Gallar, J., Dhaka, A., Viana, F., and Belmonte, C. (2010). Ocular surface wetness is regulated by TRPM8-dependent cold thermoreceptors of the cornea. Nat. Med. *16*, 1396–1399.

Peier, A.M., Moqrich, A., Hergarden, A.C., Reeve, A.J., Andersson, D.A., Story, G.M., Earley, T.J., Dragoni, I., McIntyre, P., Bevan, S., and Patapoutian, A. (2002). A TRP channel that senses cold stimuli and menthol. Cell *108*, 705–715.

Pertusa, M., Madrid, R., Morenilla-Palao, C., Belmonte, C., and Viana, F. (2012). N-glycosylation of TRPM8 ion channels modulates temperature sensitivity of cold thermoreceptor neurons. J. Biol. Chem. *287*, 18218–18229.

Pertusa, M., González, A., Hardy, P., Madrid, R., and Viana, F. (2014). Bidirectional modulation of thermal and chemical sensitivity of TRPM8 channels by the initial region of the N-terminal domain. J. Biol. Chem. *289*, 21828–21843.

Pertusa, M., Rivera, B., González, A., Ugarte, G., and Madrid, R. (2018). Critical role of the pore domain in the cold response of TRPM8 channels identified by ortholog functional comparison. J. Biol. Chem. *293*, 12454–12471.

Pierce, J.P., Mayer, T., and McCarthy, J.B. (2001). Evidence for a satellite secretory pathway in neuronal dendritic spines. Curr. Biol. *11*, 351–355.

Piña, R., Ugarte, G., Campos, M., Íñigo-Portugués, A., Olivares, E., Orio, P., Belmonte, C., Bacigalupo, J., and Madrid, R. (2019). Role of TRPM8 channels in altered cold sensitivity of corneal primary sensory neurons induced by axonal damage. J. Neurosci. *39*, 8177–8192.

Ramírez, O., García, A., Rojas, R., Couve, A., and Härtel, S. (2010). Confined displacement algorithm determines true and random colocalization in fluorescence microscopy. J. Microsc. *239*, 173–183.

Roquemore, E.P., and Banting, G. (1998). Efficient trafficking of TGN38 from the endosome to the *trans*-Golgi network requires a free hydroxyl group at position 331 in the cytosolic domain. Mol. Biol. Cell *9*, 2125–2144.

Sáenz, J.B., Sun, W.J., Chang, J.W., Li, J., Bursulaya, B., Gray, N.S., and Haslam, D.B. (2009). Golgicide A reveals essential roles for GBF1 in Golgi assembly and function. Nat. Chem. Biol. *5*, 157–165.

Saijilafu, H., Hur, E.M., and Zhou, F.Q. (2011). Genetic dissection of axon regeneration via *in vivo* electroporation of adult mouse sensory neurons. Nat. Commun. *2*, 543.

Sotelo-Silveira, J.R., Calliari, A., Kun, A., Elizondo, V., Canclini, L., and Sotelo, J.R. (2011). Localization of mRNA in vertebrate axonal compartments by *in situ* hybridization. Methods Mol. Biol. *714*, 125–138.

Szul, T., Garcia-Mata, R., Brandon, E., Shestopal, S., Alvarez, C., and Sztul, E. (2005). Dissection of membrane dynamics of the ARF-guanine nucleotide exchange factor GBF1. Traffic *6*, 374–385.

Toro, C.A., Eger, S., Veliz, L., Sotelo-Hitschfeld, P., Cabezas, D., Castro, M.A., Zimmermann, K., and Brauchi, S. (2015). Agonist-dependent modulation of cell surface expression of the cold receptor TRPM8. J. Neurosci. *35*, 571–582.

Tortosa, E., Adolfs, Y., Fukata, M., Pasterkamp, R.J., Kapitein, L.C., and Hoogenraad, C.C. (2017). Dynamic Palmitoylation Targets MAP6 to the Axon to Promote Microtubule Stabilization during Neuronal Polarization. Neuron *94*, 809–825.

Tsukita, S., and Ishikawa, H. (1976). Three-dimensional distribution of smooth endoplasmic reticulum in myelinated axons. J. Electron Microsc. (Tokyo) *25*, 141–149.

Veliz, L.A., Toro, C.A., Vivar, J.P., Arias, L.A., Villegas, J., Castro, M.A., and Brauchi, S. (2010). Near-membrane dynamics and capture of TRPM8 channels within transient confinement domains. PLoS ONE *5*, e13290.

Wang, J., Fresquez, T., Kandachar, V., and Deretic, D. (2017). The Arf GEF GBF1 and Arf4 synergize with the sensory receptor cargo, rhodopsin, to regulate ciliary membrane trafficking. J. Cell Sci. *130*, 3975–3987.

Winckler, B., and Yap, C.C. (2011). Endocytosis and endosomes at the crossroads of regulating trafficking of axon outgrowth-modifying receptors. Traffic *12*, 1099–1108.

Wu, Y., Whiteus, C., Xu, C.S., Hayworth, K.J., Weinberg, R.J., Hess, H.F., and De Camilli, P. (2017). Contacts between the endoplasmic reticulum and other membranes in neurons. Proc. Natl. Acad. Sci. USA *114*, E4859–E4867.

Xing, H., Chen, M., Ling, J., Tan, W., and Gu, J.G. (2007). TRPM8 mechanism of cold allodynia after chronic nerve injury. J. Neurosci. *27*, 13680–13690.

Ye, B., Zhang, Y., Song, W., Younger, S.H., Jan, L.Y., and Jan, Y.N. (2007). Growing dendrites and axons differ in their reliance on the secretory pathway. Cell *130*, 717–729.

Zhang, X., and Wang, Y. (2016). Glycosylation Quality Control by the Golgi Structure. J. Mol. Biol. *428*, 3183–3193.

Zheng, J.Q., Kelly, T.K., Chang, B., Ryazantsev, S., Rajasekaran, A.K., Martin, K.C., and Twiss, J.L. (2001). A functional role for intra-axonal protein synthesis during axonal regeneration from adult sensory neurons. J. Neurosci. *21*, 9291–9303.

STAR★METHODS

KEY RESOURCES TABLE

REAGENT or RESOURCE	SOURCE	IDENTIFIER
Antibodies		
Recombinant Anti-TRPM8 antibody	Abcam	Cat# ab109308; RRID:AB_10861114
Mouse anti-β-III tubulin	Santa Cruz Biotechnology	Cat# sc-80016; RRID:AB_2210523
Mouse anti-MYC	Santa Cruz Biotechnology	Cat# sc-40; RRID:AB_627268
Rat anti-LAMP1	Abcam	Cat# ab25245; RRID:AB_449893
Sheep anti-TGN38	Novus Biological	Cat# NBP1-20263; RRID:AB_1643185
rabbit anti-GBF1	Abcam	Cat# ab189512
rabbit anti-Calneuron 2	Abnova	Cat# PAB19283; RRID:AB_10902305
rabbit anti-RAB6	Cell Signaling	Cat# 9625; RRID:AB_10971791
chicken anti-Neurofilament	Millipore	Cat# AB5735; RRID:AB_240806
FITC conjugated secondary antibody	Jackson Laboratory	Cat# 711-095-152 and 703-095-155; RRID:AB_2315776 and AB_2340356
TRITC conjugated secondary antibody	Jackson Laboratory	Cat# 711-025-152, 715 and 025-150; RRID:AB_2340588 and AB_2340635
Cy5 conjugated secondary antibody	Jackson Laboratory	Cat# 711-175-152 and 703-175-155; RRID:AB_2340607 and AB_2340365
Cy3 conjugated secondary antibody	Jackson Laboratory	Cat# 703-165-155; RRID:AB_2340363
Alexa488 conjugated secondary antibody	Jackson Laboratory	Cat# 713-545-003; RRID:AB_2340744
Chemicals, Peptides, and Recombinant Proteins		
Golgicide A	Sigma	Cat# B7651
Anisomycin	Sigma	Cat# A9789
Cycloheximide	Calbiochem	Cat# 239764
Dimethyl sulfoxide	Merk	Cat# K15766131
Menthol	Sigma	Cat# 266523
WS-12	Tocris Bioscience	Cat# 3040
Fura-2 AM	Thermo Fisher	Cat# F1221
Pluronic	Thermo Fisher	Cat# P6867
Lipofectamine 3000	Thermo Fisher	Cat# L3000
DAPI	Thermo Fisher	Cat# 622348
Experimental Models: Cell Lines		
HEK293 cells	ATCC	Cat# CRL-1573
HEK293 TRPM8-myc cells	Pertusa et al., 2014	N/A
HeLa cell	ATTC	Cat# CCL-2
Experimental Models: Organisms/Strains		
Mouse BALB/cJ	Jackson Laboratory	N/A
Mouse (wild type, C57BL/6J)	Jackson Laboratory	N/A
Recombinant DNA		
Mouse TRPM8-myc	Pertusa et al., 2014, 2018	N/A
Mouse TRPM8-YFP	Pertusa et al., 2014	N/A
TGN38-mCherry	Addgene	Cat# 55145
CIB1-FusionRed-RAB6a	Nguyen et al., 2016	N/A
CRY2-mCitrine	Nguyen et al., 2016	N/A
pEGFP	Clontech	N/A
pFusionRepEGFP	Clontech	N/A
GBF1-EGFP-E794K	Szul et al., 2005	N/A

(*Continued on next page*)

Continued

REAGENT or RESOURCE	SOURCE	IDENTIFIER
pGolt-mCherry	Addgene	Cat# 73297
LAMP1-EGFP	Sebastian Brauchi (Universidad Austral, Chile)	N/A
LAMP1-mCherry	Patricia Burgos (Universidad San Sebastian, Chile)	N/A
RAB6-YFP	Gonzalo Mardones (Universidad San Sebastian, Chile)	N/A
Software and Algorithms		
ImageJ	NIH	http://imagej.net/ImageJ
Jacob plugging ImageJ	http://imagej.nih.gov/ij/plugins/track/jacob2.html	N/A
Huygens Scripting Software	Scientific Volume Imaging	N/A
IDL Workbech 7.0	ITT Visual Information Solutions	N/A
MATLAB R2012a	Math Works	N/A
GraphPad Prism 5.0a	GraphPad	N/A
pClamp 9 software	Molecular Devices	N/A
HCImage version 2	Hamamatsu Photonics	N/A
Other		
2-compartments silicone microfluidic devices	Xona microfluidics	Cat# 3000

LEAD CONTACT AND MATERIALS AVAILABILITY

Further information and requests for resources and reagents should be directed to and will be fulfilled by the Lead Contact, Andres Couve (acouve@uchile.cl). This study did not generate new unique reagents.

EXPERIMENTAL MODEL AND SUBJECT DETAILS

Animals

The Institutional Bioethics Committees from Universidad de Chile and Universidad de Santiago de Chile approved all experimental protocols involving animals. Animals in this study were housed in a 12 h light/dark cycle at 25°C, with food and water available *ad libitum*. Extracellular recordings of nerve terminals were performed on male young adult BALB/cJ mice (P30-P40). Identical results are obtained with C57BL/6J, which were used for other procedures. For trigeminal ganglia or DRG primary neuronal cultures, nerve histology, *in vivo* DRG electroporation, *ex vivo* treatments of sciatic nerves, behavioral tests, male young adult C57BL/6 mice (P30-P40) were used. Experimental groups for behavioral tests were littermates of the same sex.

Cell Cultures

HEK293 cells and a HEK293 cell line stably expressing mouse TRPM8-myc (Pertusa et al., 2014) were cultured in Dulbecco's modified Eagles medium (DMEM) supplemented with 5% or 10% fetal bovine serum (Life Technologies), 2 mM glutamine and 600 μM of geneticin (for stable lines). HeLa cells were grown in DMEM medium supplemented with 10% fetal bovine serum, 100 U/ml penicillin/streptomycin and 2 mM glutamine. Primary cultures were maintained in cultured in Minimum Essential Media (MEM) supplemented with 10% fetal bovine serum, Pen/Strep 100 μg/mL, MEM-vit (GIBCO), and nerve growth factor (100 ng/ml; Sigma-Aldrich). All cell cultures were grown at 37°C and 5% CO_2.

METHOD DETAILS

Extracellular recording of nerve terminals

Animals were euthanized with CO_2 and quickly decapitated. Eyes were carefully enucleated and placed into the recording chamber. Firing of single cold thermoreceptor neurons at the corneal surface was recorded as reported previously (Parra et al., 2010). Briefly, the excised eyes were placed in the recording chamber and secured by application of slight suction to a tube connected to the conical bottom. Eyes were continuously perfused (1 mL/min) with a recording solution containing (in mM): 128 NaCl, 5 KCl, 1 NaH2PO4, 26 $NaHCO_3$, 2.4 $CaCl_2$, 1.3 $MgCl_2$ and 10 glucose. The solution was continuously gassed with a mix of O_2 (95%) and CO_2 (5%) and maintained at the desired temperature with a computer-controlled CS-1 Peltier system (Cool Solutions), with the outlet located at the entrance of the chamber. To record nerve terminal impulses, glass micropipette electrodes (tip diameter ~50 μm) filled with the same solution were applied to the corneal surface with light suction. CTNs were identified by their ongoing

activity at 33°C, which is increased by cooling of the recording solution. Voltage signals were amplified with an AC amplifier (A-M Systems 1800; gain 10,000; low cut-off 1 Hz; high cut-off 10 KHz). Data were captured at 33.3 KHz with a Digidata 1322a interface, coupled to a computer running pClamp 9 software (Molecular Devices). Temperature was measured at the corneal surface using a BAT-12 microprobe thermometer (Physitemp) supplemented with an IT-18 thermocouple, and acquired simultaneously with voltage signals.

Trigeminal ganglia and DRG neuronal cultures

Animals were euthanized by exposure to CO_2 and decapitated. Trigeminal neurons were cultured as described previously (Madrid et al., 2006). Briefly, mouse trigeminal ganglia were dissected out in cold HBSS and incubated with collagenase XI (0,66 mg/mL) and Dispase II (3 mg/mL) (Sigma-Aldrich) in an INC-mix solution (in mM: 155 NaCl; 1.5 K_2HPO_4; 10 HEPES; 5 glucose; at pH 7,4). The enzymatic digestion was performed for 45 min at 37°C in 5% CO_2, and cells were cultured in Minimum Essential Media (MEM) supplemented with 10% fetal bovine serum, Pen/Strep 100 μg/mL, MEM-vit (GIBCO), and nerve growth factor (100 ng/ml; Sigma-Aldrich). Similar protocol was used for DRG primary cultures (González et al., 2016). Dissected DRG were dissociated with collagenase A (1 mg/ml) for 90 min and then cultured in MEM media. Cells were plated on 12 mm poly-l-lysine-coated glass coverslips and used after 3 d for immunofluorescence analysis. Alternatively, primary cultures were seed on 2-compartment silicone microfluidic devices (Xona microfluidics).

Cell line experiments

Cells were transfected with Lipofectamine 3000 (Life Technologies) according to manufacturer protocols, using 1 μg of plasmid per well on a 6-well plate format. Cells were fixed in 4% paraformaldehyde in PBS for 15 min and processed for immunofluorescence analysis.

Calcium imaging

For ratiometric Ca^{2+} imaging experiments, HEK293 stably expressing TRPM8-myc cells and HEK293 transiently transfected with TRPM8-YFP were incubated with 5 μM Fura-2 AM (F1221, Thermo Fisher Scientific) dissolved in standard extracellular solution supplemented with 0.02% Pluronic (P6867, Thermo Fisher Scientific) for 50 min at 37°C in darkness. Fluorescence measurements were made with an inverted Nikon Ti microscope fitted with a 12-bit cooled ORCA C8484-03G02 CCD camera (Hamamatsu). Fura-2 was excited at 340 and 380 nm at 0.5 Hz with a Polychrome V monochromator (Till Photonics), with exposure time no longer than 40 ms, and the emitted fluorescence was filtered with a 510 nm long-pass filter. Calibrated ratios were displayed online with HCImage version 2 software (Hamamatsu). Bath was sampled simultaneously using a BAT-12 microprobe thermometer (Physitemp Instruments) supplemented with an IT-18 T-thermocouple, using Clampex software (Molecular Devices), and digitized with an Axon Digidata 1440A AD converter (Molecular Devices).

In vivo DRG electroporation

In vivo mouse DRG electroporation of third and fourth left lumbar vertebrae ganglia (L3 and L4) was performed as previously described (González et al., 2016; Saijilafu et al., 2011). For all surgical procedures, C57BL/6 young adult mice were anesthetized with oxygen and isoflurane (Forene) [2%–3% (vol/vol)]. To expose the L3 and L4 DRGs, a small dorsolateral laminectomy was performed. For purified plasmid DNA injection, pulled capillary glass tubes were used. Electroporation was performed with custom-made tweezer electrodes. In order to reduce the inflammatory response and for analgesia, animals were subcutaneous injected with 5 mg/kg ketoprofen before surgery and for three days after every 24 h. DRG and corresponding peripheral innervation (30 mm fragments from the ganglia) were extracted 7 or 14 d after surgery.

Immunofluorescence of dissociated axons

Anesthetized animals were perfused via the left ventricle with fixative solution containing 4% paraformaldehyde. Sciatic or trigeminal nerves were removed, post-fixed for 1 h and washed with PBS. Teased fibers were incubated in 2% Triton X-100 for 2 h and blocked with 5% cold water fish jelly for 2 h. Samples were observed and analyzed on an Olympus FluoView FV1000 confocal microscope with a UPLSAPO 60x/1.35 NA objective, 4x digital zoom, KALMAN 2, and Z longitudinal section of 0.2 μm (10-12 optical slices for each axon). In all experiments, images considered for analysis originate from at least three different animals.

Ex vivo treatments of sciatic nerves

Animals were euthanized by exposure to CO_2. Sciatic nerves were exposed and excised (Sotelo-Silveira et al., 2011). Segments were cultured in DMEM F12 (GIBCO) and treated with GCA (20 μM). Dimethyl sulfoxide (0.002%) was used as vehicle and control for GCA. After 1 h, sciatic nerves were washed and fixed for an additional 1 h in 4% paraformaldehyde. Fibers were teased and processed for immunofluorescence as described previously (González et al., 2016; Zheng et al., 2001). Experimental settings for morphology and colocalization analysis consider each confocal Z stack, extracted from at least three animals per condition, as a single experimental sample (n).

Morphology analysis of secretory structures

Analysis of particles in the axonal compartment was carried out using a local maximum algorithm developed in MATLAB R2012a (Mathworks). Briefly, particles were segmented using a binary mask considering the fluorescence intensity of each structure relative

to its surroundings. A minimum threshold of 40 arbitrary units (a.u.) (range 1-255 a.u.) and a minimum intensity difference of 35 a.u. (particle/surrounding) were used. Segmented images were analyzed using ImageJ (NIH). Number and area of particles were obtained using the same tool.

Colocalization analysis

Co-localization analysis was performed as described previously (Ramírez et al., 2010). Briefly, samples were acquired on a confocal microscope (Fluoview FV1000) using a UPLSAPO 60x/1.35 NA objective, 4x digital zoom and KALMAN 2. An average of 10 confocal images per sample were considered in the analysis (0.2 μm thickness each). We guaranteed that images did not saturate and that image background was slightly above zero. Image stacks were deconvolved with Huygens Scripting Software (SVI, Hilversum, The Nertherlands) using an algorithm based on the classic maximum likelihood estimator (CMLE). The signal-to-noise ratio was adjusted until the deconvolved images were free of pixel noise. Images were segmented using IDL Workbech 7.0 (ITT Visual Information Solutions, USA). Alternatively, channels were segmented using a series of ImageJ software filters to obtain masked images with JaCob pluggin to simplify the analysis of *in vitro* experiments. The ratio of colocalization between two signals was calculated using Mander's coefficients and a confined displacement algorithm that determines true and random colocalization. As a result, Mander's coefficients, M1 and M2, were expressed as percentage of true colocalization.

Time-lapse fluorescence microscopy

HeLa cells grown on glass bottom Fluorodishes were transiently transfected with GBF1-EGFP and RAB6a-mCherry or RAB6a'-mCherry using X-tremeGENE9 (Roche) following manufacturer's instructions. Time-lapse imaging was performed at 37°C using an inverted and motorized spinning-disk microscope (Nikon TE2000-U) through a 100x1.4NA PL-APO objective lens. The apparatus is composed of a Yokogawa CSU-22 spinning disk head, a Roper Scientific laser launch, a Photometrics Coolsnap HQ2 CCD camera for image acquisition and Metamorph software (MDS) to control the setup. Acquisition parameters were 100 msec exposure for EGFP and mCherry channels. Laser was set to 40%. Images correspond to the maximal intensity projection through the Z axis performed with the ImageJ software.

Yeast two-hybrid experiments

Yeast two hybrid (Y2H) experiments were performed as described previously (Miserey-Lenkei et al., 2010), except that the GAD-fusion proteins correspond to different domains of GBF1.

Aversive cold-plate test

Selected two-month-old male C57BL/6 mice that showed aversive behavior in a cold-plate test at 0°C were *in vivo* DRG co-electroporated with CIB1-FusionRed-RAB6a and CRY2-mCitrine or EGFP. Behavioral experiments were tested blindly. Two weeks after electroporation animals were evaluated for cold sensitivity. Briefly, mice were placed in the experimental room and acclimated for 1 h with regular illumination. After a first cold sensitivity test, 5% lidocaine was applied topically to the contralateral right hindpaw and a second test was performed after 30 min in the dark. Animals were then illuminated with a blue LED lamp (470 nm) located at the bottom of the cage for 30 min and the final test was performed. For each cold sensitivity test the plate was set to 0°C and each trial ended when the animal jumped displaying escape behavior, or reached a maximum of 59 s in the plate without aversive response. We quantified the latency to jump, and when animals did not jump, the maximum latency time of recording was assumed for quantification. Mean latency was calculated as the average of 3 consecutive days following the identical protocols.

Menthol-sensitized cold-plate test

Two-month-old male C57BL/6 mice were *in vivo* DRG co-electroporated with CIB1-FusionRed-RAB6a and CRY2-mCitrine or EGFP. Two weeks after electroporation animals were evaluated for cold sensitivity. Briefly, mice were placed in the experimental room and acclimated for 1 h with regular illumination. After a first cold sensitivity test, 5% lidocaine was applied topically to the contralateral right hindpaw. Then, 6% menthol was applied topically to the ipsilateral left hindpaw to induce menthol-evoked sensitization, and a second test was performed after 30 min in the dark. Animals were then illuminated with a blue LED lamp (470 nm) located at the bottom of the cage for 30 min and the final test was performed just after a new menthol application. For each cold sensitivity test the plate was set to 10°C. Video recordings of animals were performed and offline scoring was assigned by double blind. The number of the following cold-response events of the electroporated left lower limb were monitored over the following 60 s and an arbitrary score was assigned to the behavior: 0 indicated no response, 1 lifting response and 2 for licking, brushing or jump. Total number of responses was summed. Three trials were obtained from each animal in three consecutive days to obtain a mean score by each animal. 6% (wt/wt) menthol was dissolved in petroleum jelly (Vaseline) and applied topically the plantar surface of the hindpaw, in a volume of ~50 μL using a cotton swab.

Hot-plate test

This test was performed in the same conditions described for aversive cold-plate test. For heat sensitivity test the plate was set to 55°C (cutoff time 20 s). Time before the first aversive response in seconds was quantified. Aversive response was defined as a lifting, flicking or licking of hindpaw.

QUANTIFICATION AND STATISTICAL ANALYSIS

Plots and data analysis were performed using GraphPad Prism 5.0a software. For particle size analysis box-and-whisker-plots were used to represent the total population of particle area (Figure 2; Figures S2 and S4). Disaggregates statistical analysis by quartile (Q1 to Q4) of each marker were presented as a supplementary figure (Figure S4). Two segment Y-axes were chosen in the main graphs to guarantee optimal visualization of relevant differences per quartile (Figure S4F).

Statistical details are found in each figure legends. In general, group data are expressed as mean ± sem. Shapiro-Wilk was used for normality test. Student's unpaired or paired t test, and one-way analysis of variance (ANOVA) with Tukey's post-test were used for comparing parametric groups. For nonparametric analysis, Mann-Whitney and Kruskal-Wallis or Friedman tests with Dunns post-test were used. Differences between two or more groups were considered significant when $*p < 0.05$, $**p < 0.01$ and $***p < 0.001$.

DATA CODE AND AVAILABILITY

This study did not generate any datasets. All data will be made available from the corresponding author on request.